

# Topographic stress and rock fracture: a two-dimensional numerical model for arbitrary topography and preliminary comparison with borehole observations

Mirna Slim,<sup>1</sup> J. Taylor Perron,<sup>1\*</sup> Stephen J. Martel<sup>2</sup> and Kamini Singha<sup>3</sup>

<sup>1</sup> Department of Earth, Atmospheric and Planetary Sciences, Massachusetts Institute of Technology, Cambridge, Massachusetts, USA

<sup>2</sup> Department of Geology and Geophysics, University of Hawaii, Honolulu, Hawaii, USA

<sup>3</sup> Hydrologic Science and Engineering Program, Colorado School of Mines, Golden, Colorado, USA

Received 19 February 2014; Revised 31 July 2014; Accepted 18 August 2014

\*Correspondence to: J. Taylor Perron, 77 Massachusetts Avenue, 54-1022, Cambridge, MA 02139, USA. E-mail: perron@mit.edu

# ESPL

Earth Surface Processes and Landforms

**ABSTRACT:** Theoretical calculations indicate that elastic stresses induced by surface topography may be large enough in some landscapes to fracture rocks, which in turn could influence slope stability, erosion rates, and bedrock hydrologic properties. These calculations typically have involved idealized topographic profiles, with few direct comparisons of predicted topographic stresses and observed fractures at specific field sites. We use a numerical model to calculate the stresses induced by measured topographic profiles and compare the calculated stress field with fractures observed in shallow boreholes. The model uses a boundary element method to calculate the stress distribution beneath an arbitrary topographic profile in the presence of ambient tectonic stress. When applied to a topographic profile across the Susquehanna Shale Hills Critical Zone Observatory in central Pennsylvania, the model predicts where shear fractures would occur based on a Mohr–Coulomb criterion, with considerable differences in profiles of stresses with depth beneath ridgetops and valley floors. We calculate the minimum cohesion required to prevent shear failure,  $C_{\min}$ , as a proxy for the potential for fracturing or reactivation of existing fractures. We compare depth profiles of  $C_{\min}$  with structural analyses of image logs from four boreholes located on the valley floor, and find that fracture abundance declines sharply with depth in the uppermost 15 m of the bedrock, consistent with the modeled profile of  $C_{\min}$ . In contrast,  $C_{\min}$  increases with depth at comparable depths below ridgetops, suggesting that ridgetop fracture abundance patterns may differ if topographic stresses are indeed important. Thus, the present results are consistent with the hypothesis that topography can influence subsurface rock fracture patterns and provide a basis for further observational tests. Copyright © 2014 John Wiley & Sons, Ltd.

**KEYWORDS:** topographic stress; fracture; boundary element method; critical zone; Susquehanna Shale Hills Observatory

## Introduction

### Motivation and purpose

Fractures in bedrock influence numerous processes that drive landscape evolution, including weathering (Anderson *et al.*, 2007), erosion (Moon and Selby, 1983; Augustinus, 1995; Whipple *et al.*, 2000; Molnar *et al.*, 2007; Moore *et al.*, 2009; Dühnforth *et al.*, 2010), slope stability (Terzaghi, 1962; Wiczorek and Snyder, 1999; Muller and Martel, 2000; Chigara, 2000; Clarke and Burbank, 2010, 2011; Stock *et al.*, 2012), and groundwater flow (LeGrand, 1949; Keller *et al.*, 1986; Trainer, 1988; Borchers, 1996; Berkowitz, 2002; Neuman, 2005). Various studies have suggested that landforms might in turn influence bedrock fractures by perturbing the ambient stress field (McTigue and Mei, 1981; Savage *et al.*, 1985; Savage and Swolfs, 1986) and altering the type, orientation and abundance of fractures in different parts of the subsurface (Miller and Dunne, 1996). This mutual influence could

lead to feedbacks between evolving topography and fracture patterns (Miller and Dunne, 1996; Molnar, 2004). However, few studies have tested whether modeled topographic stresses appear to have influenced observed bedrock fracture patterns, in part because prior theoretical approaches were too simplified to apply to specific topographic and tectonic settings. This paper has two purposes: (1) to provide a modeling framework for calculating topographic stresses beneath arbitrary topography subject to approximately two-dimensional (plane-strain) conditions; and (2) to conduct a preliminary test for the effects of topographic stresses by comparing a stress model for a specific field site with fractures observed in shallow boreholes.

### Previous studies of topographic stress and rock fracture

Early studies of topographic stresses focused on the effects of large-scale topography (hundreds of kilometers or more in

horizontal extent) on the lithosphere at depths of kilometers or more (see review in McNutt, 1980). Holzhausen (1977) and McTigue and Mei (1981) were among the first to study the stress distribution immediately beneath local topographic features. Holzhausen (1977) examined an elastic medium with a gently sloping sinusoidal surface using a perturbation method. McTigue and Mei (1981) also used a perturbation method valid for gently sloping surfaces but considered more complex topographic forms with the aid of a spectral approach. McTigue and Mei (1981) used these approximate solutions to show that even if regional horizontal stresses are absent, topography induces horizontal compression under ridgetops and horizontal tension under valley floors, and that the effect of topography decreases with depth. They also showed that the addition of regional horizontal compressive stress can induce horizontal tension at topographic highs, a result noted earlier by Scheidegger (1963).

Savage *et al.* (1985) and Savage and Swolfs (1986) subsequently found exact analytical solutions for the elastic stress distribution under certain landforms using the approach of Muskhelishvili (1953). Their solutions are valid for a set of idealized, symmetric, isolated valleys and ridges with shapes described by a conformal coordinate mapping. Savage *et al.* (1985) calculated the effect of gravity in a laterally constrained medium and showed that topographic stresses are on the order of  $\rho gb$ , where  $\rho$  is the rock density,  $g$  is the acceleration of gravity, and  $b$  is ridge height or valley depth. Like Holzhausen (1977) and McTigue and Mei (1981), Savage *et al.* (1985) predict horizontal compressive stress under ridgetops, horizontal tensile stress under valley floors, and stresses approaching those beneath a horizontal surface as depth increases. Savage and Swolfs (1986) additionally evaluated how topography perturbs a regional horizontal tectonic stress and then superposed their solutions on those of Savage *et al.* (1985) to obtain the stress distribution due to both tectonic and gravitational stresses. They demonstrated that the effect of regional tectonic compression is reduced near ridge crests and amplified in valleys. Pan and Amadei (1994) proposed a similar method that uses a numerical conformal mapping procedure to accommodate irregular but smooth two-dimensional topographic profiles.

Savage *et al.* (1985) and Savage and Swolfs (1986) calculated subsurface stresses assuming that the ratio  $k$  of the vertical gradient of horizontal stress to the vertical gradient of vertical stress was positive but less than one. Miller and Dunne (1996) compiled published crustal stress values from different geographic locations and concluded that in many places  $k > 1$ . Noting that many of the reported stresses indicated high regional compressive tectonic stress, they used the approach of Savage *et al.* (1985) and Savage and Swolfs (1986) to calculate stresses for cases with  $0 < k < 1$  and  $k > 1$ . They also noted that the magnitudes of the modeled stresses exceeded typical mechanical strengths of various rock types, and used brittle fracture criteria based on laboratory experiments to predict the fracture patterns that would develop for different combinations of landform shape and tectonic stress state.

Miller and Dunne (1996) discussed the implications of their fracture predictions for landscape evolution. Noting that elastic stresses scale with topographic relief, they proposed that fracturing might occur only if the topographic relief (ridge height above valley floor) is sufficiently high that the stresses exceed a brittle failure threshold. They also proposed a positive feedback between topographic stresses and landscape evolution in which valley incision triggers fracturing in the valley floor, which makes bedrock more erodible, accelerates valley incision, and further enhances the fracturing effect. Molnar (2004) revisited the examples discussed by both Savage *et al.* (1985) and Miller and Dunne (1996). He developed a framework for quantifying the positive feedback in sustaining a valley that

Miller and Dunne (1996) proposed, and showed the dependence of stress concentration in a valley on its shape, especially the sharpness of the 'V' at the valley axis. Molnar (2004) also suggested that static fatigue (gradual crack growth at stresses below the macroscopic failure threshold) could be an important mechanism by which topographic stresses influence rock erodibility and landscape evolution.

These studies have advanced our understanding of topographic stresses and the possible consequences for landscape evolution, but only a few investigations have compared these predictions with observed stresses, fracture patterns, or proxies for rock damage. Savage and Morin (2002) and Morin and Savage (2002) used the analytical solutions of Savage *et al.* (1985) to approximate the near-surface stresses at a study site in the Davis Mountains of Texas, and compared their predictions with stress orientations inferred from borehole breakouts. They found that breakout orientation appeared to change with depth in a manner consistent with their stress calculations. However, they did not attempt to compare predicted stresses with fracture patterns. Morin *et al.* (2006) processed sonic logs and borehole images to study the mechanical properties of a fractured basalt aquifer and the permeability of subsurface fractures. They used a two-dimensional finite element model to calculate the stress distribution beneath the Annapolis Valley, Nova Scotia, and found that topographic stresses appear to influence the permeability of pre-existing fractures. Martel (2011) predicted the areal distribution of sheeting joints in part of Yosemite National Park using an exact solution for the gradient in the normal stress perpendicular to the surface. He accounted for the site-specific topography but assumed the surface-parallel compressive stresses were constant. Observations of sheeting joints on domes, ridges, and saddles with wavelengths of a few hundred meters were consistent with the hypothesis that surface-parallel stresses and topography account for the formation of sheeting joints (Martel, 2011). Leith *et al.* (2013a) applied a model of coupled stress and elasto-plastic rock deformation (Leith *et al.*, 2013b) to the Matter Valley in the Swiss Alps, and found that a zone where the model predicts extensional fracturing corresponds to a break in slope on the valley walls where enhanced glacial erosion has created an inset U-shaped gorge. However, they did not attempt to compare their model systematically with rock fracture patterns. An opening clearly exists for a more complete examination of the coupling between topography and stress state, the importance of this coupling at depth, and the combined impact on fractures at a specific site.

## New contribution and outline

In this paper, we implement a numerical method for calculating stresses beneath topographic profiles of arbitrary form and compare predicted topographic stresses with fracture patterns mapped from shallow boreholes. We first describe our adaptation of the boundary element model of Martel (2000) and Martel and Muller (2000), which calculates two-dimensional elastic stresses due to the combined effects of ambient tectonic stress and gravity acting on topography. We then apply the model to idealized, synthetic topographic profiles to illustrate the sensitivity of calculated stresses and fracture patterns to tectonic stress, rock mechanical parameters, and the shapes of ridges and valleys. Next, we calculate stresses beneath a topographic profile across the Shale Hills, an experimental watershed in central Pennsylvania. We use the modeled stresses to calculate a proxy for shear fracture susceptibility and compare that proxy with the fracture abundance observed in optical logs of shallow boreholes in the valley floor. Finally, we comment on the implications of our results for the hypothesized effects

of topographic stress on rock fracture, and we discuss shortcomings in our current understanding of rock damage accumulation that must be addressed to fully characterize the influence of stress on landscape evolution.

## Boundary element model for stresses induced by arbitrary topography

### Model description

The need to study stresses induced by real topography and their interactions with variable tectonic stresses motivated Martel and Muller (2000) to develop a flexible numerical method. They adapted a boundary element method (BEM) based on Crouch and Starfield's (1983) two-dimensional displacement discontinuity code (TWODD), which is in turn based on an analytical solution for a constant discontinuity displacement over a finite linear segment in an infinite, two-dimensional elastic solid. A typical application of Crouch and Starfield's (1983) method is to calculate the stresses around a crack in a body of rock. The crack is approximated by a set of linear segments, and the displacement discontinuity – opening, closing and/or sliding – across the crack is approximated by a set of discrete displacement discontinuities across the linear segments. Normal and shear tractions on the linear segments are specified as boundary conditions. The TWODD code then solves for the displacements on opposing sides of the linear segments that satisfy these boundary conditions. Once these displacements are known, the resulting stresses at any point in the body of rock can be calculated. This solution method can account for an arbitrary ambient horizontal stress field.

Martel and Muller (2000) adapted the method of Crouch and Starfield (1983) by treating a topographic surface as a long, traction-free crack in a body of rock that is exhumed by the removal of overburden. We adopt and extend their method here. In this section, we give an overview of the computational procedure; for a more detailed explanation, see Martel and Muller (2000) and Crouch and Starfield (1983). The topographic surface is approximated by a set of connected, traction-free linear segments passing through a laterally confined body in plane strain under the influence of gravity (Figure 1). The ambient stresses in this body are

$$\sigma_{xx}^a = k \rho g y + \sigma_{xx}^t \quad (1a)$$

$$\sigma_{yy}^a = \rho g y \quad (1b)$$

$$\sigma_{xy}^a = \sigma_{yx}^a = 0 \quad (1c)$$

where  $x$  is the horizontal coordinate (increasing to the right),  $y$  is the vertical coordinate (increasing upward),  $\rho$  is rock density,  $g$  is gravitational acceleration, and stress subscripts use the 'on-in' convention (Pollard and Fletcher, 2005). Compressive stresses are defined as negative. The term  $\sigma_{xx}^t$  in Equation (1a) is a constant ambient horizontal tectonic stress that may exist in addition to the gravitationally induced stresses. The parameter  $k$  scales the vertical gradient in the ambient horizontal normal stress relative to the vertical gradient in the ambient vertical normal stress. We use  $k$  rather than the term  $\nu/(1-\nu)$ , where  $\nu$  is Poisson's ratio, to emphasize that the in-plane stress solutions are independent of the elastic parameters of the rock, provided it is homogeneous and isotropic (Timoshenko and Goodier, 1970).

The stress field below the topographic surface is found by evaluating the stress perturbation caused by the generation of the topography (via the erosion of overburden) and then superposing this perturbation on the ambient stress field. The shear tractions,  $\sigma_s$ , and normal tractions,  $\sigma_n$ , on the elements defining the topographic surface are set to zero. This traction-free condition does not necessarily imply a stress-free surface, because the surface-parallel normal stress can be nonzero. The ambient stresses at the element locations due to the overburden are calculated from Equation 1(a)–(c), resolved into shear and normal tractions, and subtracted from the zero-traction condition to define the boundary conditions for a boundary element problem describing the topographic stress perturbation (that is, they describe the effect of the topographic 'crack' on the ambient stress). The resulting tractions are stored in a vector  $\mathbf{b}$ . The TWODD method is then used to calculate a matrix  $\mathbf{A}$  of influence coefficients. Each element of  $\mathbf{A}$  gives the change in either shear or normal traction on one boundary element due to a unit shear or normal displacement discontinuity at another boundary element. This defines a system of linear equations,

$$\mathbf{A}\mathbf{x} = \mathbf{b} \quad (2)$$

which is solved to yield the unknown displacement discontinuities,  $\mathbf{x}$ , at the elements.

Once these displacement discontinuities are known, the stress perturbation at any observation point below the topographic surface can be calculated. A set of observation points is chosen, and TWODD is used to calculate a second matrix of influence coefficients,  $\mathbf{A}^{\text{obs}}$ . Each element of  $\mathbf{A}^{\text{obs}}$  gives the effect of a unit shear or normal displacement discontinuity at one of the boundary elements on the horizontal normal stress, vertical normal stress, or shear stress at one of the observation points. The total stress perturbations at the observation points,  $\sigma^{\text{obs}}$ , are calculated as

$$\mathbf{A}^{\text{obs}}\mathbf{x} = \sigma^{\text{obs}} \quad (3)$$

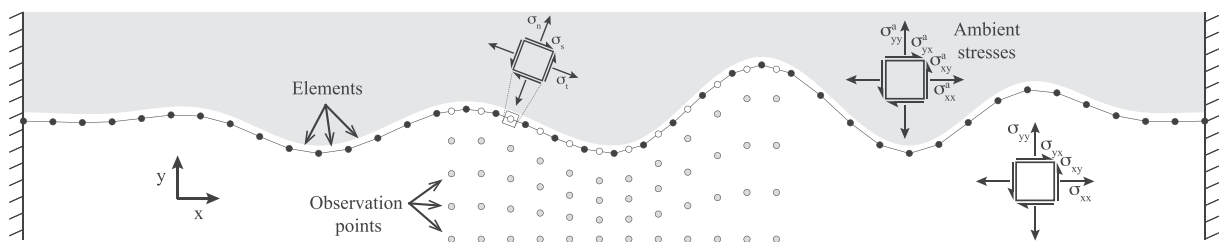


**Figure 1.** Schematic diagram illustrating the coordinate system and setup of the boundary element model. The gray region above the land surface represents the overburden that is mathematically removed from the underlying rock to generate the topographic surface. The small gap between the gray region and the land surface represents the traction-free 'crack' described by the displacement discontinuity method. Black circles represent element endpoints, white circles represent element midpoints, and gray circles represent observation points where stresses are calculated at depth. Squares with arrows show the orientations of stresses defined in the text. Hatched left and right boundaries represent lateral confinement.

The final step is to add the stress perturbations  $\mathbf{b}$  and  $\sigma^{\text{obs}}$  to the ambient stresses (Equations 1a, 1b, 1c) at the elements and the observation points, respectively. This yields the total stresses at and below a traction-free topographic surface due to gravity and any horizontal tectonic stress.

The shear and normal tractions on the elements that define the land surface are known (they are specified as boundary conditions), but the TWODD method does not calculate the surface-parallel (tangential) normal stresses on the elements. Following Crouch and Starfield (1983, section 5.10), we approximate the tangential normal stresses using finite differences. The shear and normal displacements of the elements are differenced to obtain an approximation for the tangential normal strain at each element midpoint, and the tangential stress is calculated from Hooke's Law. Along with the shear and normal tractions on the elements, this completely defines the stress field at and below the land surface.

A few additional considerations should be noted when using the TWODD method to calculate topographic stresses. To ensure an equilibrium stress state, the left and right ends of the topographic surface should be tapered to the same elevation (Figure 1). Tapering to a horizontal surface that extends beyond the area of interest (Figure 1) will minimize edge effects. The additional computational cost introduced by this tapering is not large, because longer elements can be used near the ends of the profile, and because observation points need only be chosen within the area of interest. The calculated stresses are very accurate at element midpoints and at observation points farther than an element length from element endpoints, but can be inaccurate at observation points within an element length of element endpoints. Two strategies that mitigate this effect are to center near-surface observation points beneath element midpoints and make elements short enough that the zones of inaccuracy around element endpoints only extend a short distance below the land surface.

The BEM presented here uses a very different approach to calculate topographic stresses than previous analytical methods, so it is useful to confirm that the different approaches yield equivalent results for the same scenarios. We compared BEM solutions with analytical solutions (Savage *et al.*, 1985; Savage and Swolfs, 1986) for an isolated valley with and without ambient tectonic stress (Figure 9 in Savage and Swolfs, 1986). In the analytical solutions, stresses were calculated at points evenly spaced in  $u$  and  $v$  in the coordinate mapping of Savage *et al.* (1985). In the BEM solutions, stresses were calculated at points defined with the meshing scheme described above. Parameter values are listed in Table 1. Figure 2 compares  $\sigma_{xx}$  in the analytical solutions (Figure 2(a), (b)) with the BEM solutions (Figure 2(c), (d)). The analytical and BEM solutions agree closely, consistent with the results of Martel and Muller (2000). The largest discrepancies

occur at the land surface due to the reduced accuracy of the finite-difference approximation used to calculate tangential normal stress on the boundary elements (Crouch and Starfield, 1983, section 5.10), but these discrepancies are sufficiently small that they are not apparent in Figure 2. Unlike the analytical methods, the BEM can be used to calculate stresses beneath any topographic profile, a property we exploit in this study.

## Predicting fracture mode and orientation

Given a calculated stress field, we seek to estimate the mode, orientation and abundance of any resulting fractures as a basis for comparison with observed fractures. Following Miller and Dunne (1996), we use experimentally determined criteria for opening-mode and shear failure of rock. In plane strain, two of the principal stresses are in the plane of the topographic cross-section, and the third principal stress is the normal stress perpendicular to the cross-section,  $\sigma_{zz}$ . In most of the scenarios considered here, the most compressive principal stress  $\sigma_3$  and the least compressive principal stress  $\sigma_1$  are in the plane of the cross-section,  $\sigma_{zz}$  is the intermediate principal stress, and the three are related by  $\sigma_{zz} = \nu(\sigma_1 + \sigma_3)$ . However, there are two situations in which  $\sigma_{zz}$  is not the intermediate principal stress. If  $\sigma_{lc}/\sigma_{mc} < \nu/(1-\nu)$ , where  $\sigma_{lc}$  is the least compressive in-plane principal stress and  $\sigma_{mc}$  is the most compressive in-plane principal stress, then  $\sigma_{zz}$  is the least compressive principal stress. This can only occur where both  $\sigma_{lc}$  and  $\sigma_{mc}$  are compressive. If  $\sigma_{mc}/\sigma_{lc} > \nu/(1-\nu)$ , then  $\sigma_{zz}$  is the most compressive principal stress. This can only occur where both  $\sigma_{lc}$  and  $\sigma_{mc}$  are tensile.

The well-known graphical representation of a two-dimensional stress state at a point is the Mohr circle (Figure 3). The simplest and most commonly applied shear failure criterion is the Coulomb criterion:

$$|\tau| = -\sigma \tan \phi + C \quad (4)$$

which states that the shear stress,  $\tau$ , acting on a plane at the point of shear failure equals the sum of the cohesive strength of the material,  $C$ , and the frictional resisting stress, given by the term  $-\sigma \tan \phi$ , where  $\phi$  is the internal friction angle of the material and  $\sigma$  is the normal stress acting on the failure plane. The Coulomb criterion defines a pair of linear failure envelopes that are symmetric about the  $\sigma$  axis on the Mohr diagram (Figure 3). If the Mohr circle touches this failure envelope, shear fractures can form on either of two conjugate planes with normal vectors oriented at angles  $\theta = 45^\circ + \phi/2$  with respect to the most compressive principal stress direction, such that the fractures themselves are oriented  $90^\circ - \theta = 45^\circ - \phi/2$  away from

**Table 1.** Parameters used in model calculations\*

| Figure         | $k$          | $E$ (GPa) | $\sigma_{xx}^t$ (MPa) | $C$ (MPa) | $q_u$ (MPa) | $\phi$     | $\Delta x^{\dagger}$ (m) |
|----------------|--------------|-----------|-----------------------|-----------|-------------|------------|--------------------------|
| 2 <sup>‡</sup> | 0.5          | 1         | -b to 0               |           |             |            | 0.05                     |
| 4 <sup>‡</sup> | 1.5          | 1         | 0                     | 0         | 0           | 30°        | 0.05                     |
| 5              | 0.5          | 50        | -6                    | 1         | 3           | 30°        | 5                        |
| 6              | 0.5          | 50        | -6 to +2              | 0 to 2    | 0 to 6      | 15° to 45° | 10                       |
| 7              | 0.5          | 50        | -6                    | 1         | 3           | 30°        | 10                       |
| 10             | 0.5          | 30        | -10                   | 1         | 3           | 20°        | 3.5/1.15                 |
| 11             | 0.25 to 0.67 | 30        | -10 to 0              | 1         | 3           | 10° to 30° | 3.5                      |
| 15             | 0.5          | 30        | -10                   | 1         | 3           | 20°        | 1.75                     |

\*Dimensionless calculations (Figures 2 and 4) used  $\rho g = 1$ . Dimensional calculations (Figures 5–15) used  $\rho = 2650 \text{ kg/m}^3$ ,  $g = 9.81 \text{ m/s}^2$ . All calculations used  $\sigma_{yy}^t = \sigma_{xy}^t = 0$ .

<sup>†</sup>Average horizontal spacing of element endpoints, which is shorter than but approximately equal to the average element length.

<sup>‡</sup>Units do not apply to dimensionless calculations in Figures 2 and 4.



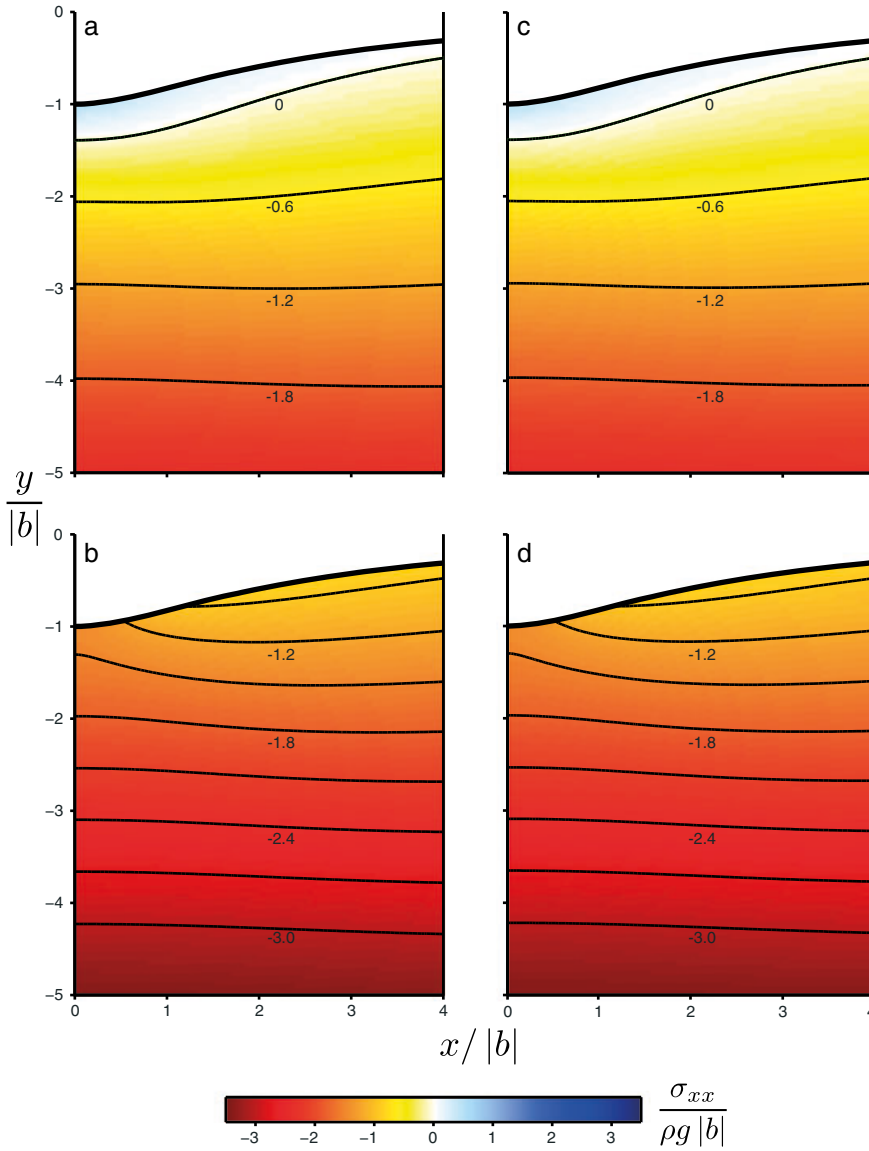


**Figure 2.** Comparison of horizontal stress in boundary element model solutions (c, d) with analytical solutions of Savage and Swolfs (1986) (a, b) for the scenarios shown in their Figure 9. The symmetric valley topography (only half of which is shown) is defined by the conformal coordinate mapping of Savage *et al.* (1985) with  $a=3$  and  $b=-1$ . The scenario in (a) and (c) has an ambient horizontal surface stress of  $\sigma_{xx}^{a,0} = 0$ , and the scenario in (b) and (d) has a compressive ambient horizontal surface stress of  $\sigma_{xx}^{a,0} = -\rho gb$ . Coordinates and stresses are normalized as indicated. Contours are stresses in the same units as the color scale. Other parameter values are listed in Table I. This figure is available in colour online at [wileyonlinelibrary.com/journal/espl](http://wileyonlinelibrary.com/journal/espl)

$\sigma_3$ . The Coulomb criterion can also be written in terms of the principal stresses (Jaeger *et al.*, 2007):

$$-\sigma_3 = 2C \tan \theta - \sigma_1 \tan^2 \theta \quad (5)$$

If pre-existing planes of weakness occur with lower cohesion or a different friction angle than intact rock, sliding (slip) on these planes may also occur. The Mohr diagram of Figure 3, which illustrates the case of pre-existing fractures with no cohesion and a friction angle  $\phi_s$ , shows that sliding would occur on any planes with normal vectors oriented at angles between  $\theta_1$  and  $\theta_2$  with respect to the most compressive principal stress.

If the normal stress on potential shear failure planes is not compressive, shear fractures typically do not occur, and the Coulomb criterion is not a relevant description of the failure mode. Laboratory experiments with low confining pressures typically produce opening-mode fractures oriented perpendicular to the least compressive (most tensile) principal stress,  $\sigma_1$  (Paterson and Wong, 2005). The transition between opening mode and shear failure is complex, and can include hybrid

fractures with characteristics of both end-member types (Ramsey and Chester, 2004). Following Miller and Dunne (1996), we use a simple approximation for the transition suggested by Jaeger *et al.* (2007). The stress state corresponding to the value of  $\sigma_3$  for which the normal stress on a potential shear failure plane ceases to be compressive can be visualized by drawing the Mohr circle that is tangent to the shear failure envelope where it crosses the  $\tau$  axis (Figure 3). From trigonometry, and using Equation (5), this implies that  $-\sigma_3 = C \tan \theta$  and  $\sigma_1 = C / \tan \theta$  (Jaeger *et al.*, 2007). Thus, shear fracture is predicted if

$$-\sigma_3 \geq C \tan \theta \text{ and } C < C_{\min} \quad (6)$$

where  $C_{\min}$  is obtained by solving for  $C$  in Equation (5),

$$C_{\min} = \frac{-\sigma_3 + \sigma_1 \tan^2 \theta}{2 \tan \theta} \quad (7)$$

and opening-mode fracture perpendicular to  $\sigma_1$  is predicted if

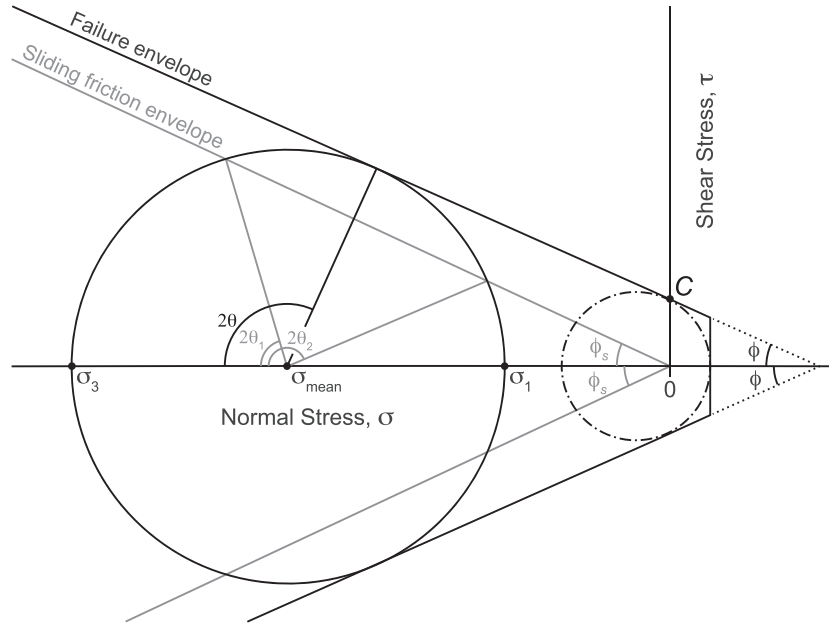


**Figure 3.** Mohr diagram for a specific stress state defined by the most compressive ( $\sigma_3$ ) and least compressive ( $\sigma_1$ ) principal stresses. Compression is negative. The value of the mean stress,  $\sigma_{mean}$ , is indicated. Quantities related to the formation of new fractures are black, and quantities related to sliding on existing fractures are gray. Dotted lines represent the extension of the shear failure envelope to the  $\sigma$  axis. Dash-dot Mohr circle represents the state of stress at which the failure criterion prescribes a transition from shear fracture to tensile fracture.

$$-\sigma_3 < C \tan \theta \text{ and } C < \sigma_1 \tan \theta \quad (8)$$

Graphically, this is equivalent to truncating the Coulomb failure envelope at  $\sigma = C/\tan \theta$  and extending the failure envelope vertically to the  $\sigma$ -axis (Figure 3). Miller and Dunne (1996) also assume that opening-mode failure occurs in unconfined compression ( $\sigma_1 = 0$ ,  $\sigma_3 < 0$ ) if  $\sigma_3$  exceeds the unconfined compressive strength of the rock,  $q_u$ . To facilitate comparisons with their results, we also use this criterion. In most of the examples considered here, unconfined compression occurs only at the land surface, so this criterion predicts surface-parallel opening-mode fractures right at the surface.

Recognizing that rocks in natural settings are typically influenced by heterogeneities that are not described by these simple failure criteria, and that rock mechanical properties are seldom known precisely, we seek an additional proxy for the likelihood of shear failure. From Equation (6), the minimum cohesion needed to prevent the development of new shear fractures at a given location in the rock is  $C_{min}$ , which is defined in Equation (7).  $C_{min}$  corresponds to the  $\tau$ -axis intercept of the failure envelope tangent to the Mohr circle that describes the state of stress. For a given friction angle  $\phi$ , larger values of  $C_{min}$  indicate that shear fractures are more likely to form and that sliding on existing fractures is more likely to occur, whereas smaller values of  $C_{min}$  indicate that shear fractures and sliding are less likely. An alternative measure proposed by Iverson and Reid (1992) is the failure potential,  $\Phi$ , defined as

$$\Phi = \frac{|\sigma_3 - \sigma_1|}{\sigma_3 + \sigma_1} \quad (9)$$

For a cohesionless material on the verge of shear failure (described by a Mohr circle tangent to a failure envelope that intercepts the origin of a plot such as Figure 3),  $\Phi = \sin \phi$ , and thus  $\Phi$  describes the internal friction needed to prevent failure of a cohesionless material.  $\Phi$  is a dimensionless, scale-independent measure of shear failure potential, whereas  $C_{min}$  is dimensional and scale-dependent. In this paper, we are most interested in dimensional topographic scenarios in which rocks

have nonzero cohesion.  $C_{min}$  is therefore a more useful proxy for our purposes, and we use it in the examples below.

Tests confirm that the fracture patterns predicted by the BEM are consistent with previous analytical approaches. We compared fracture patterns for one of the scenarios investigated by Miller and Dunne (1996), who used the analytical stress solutions of Savage *et al.* (1985) and Savage and Swolfs (1986). The scenario is a valley with no ambient horizontal compression at the far-field land surface and  $k = 1.5$  in Equation (1a), denoting a rapid increase in horizontal compression with depth (Figures 4 and 7 of Miller and Dunne, 1996). Figure 4 shows that the two approaches predict essentially identical fracture patterns, which is expected given the close agreement of the stress fields (Figure 2) and the use of the same fracture criteria.

### Sensitivity of stress and fracture patterns to model parameters and topography

An example using a simple topographic surface illustrates how differences in model parameters and topography influence the calculated stress field and predicted fractures. We used the BEM to calculate stresses at and beneath a sinusoidal topographic profile with a wavelength of 500 m, an amplitude of 50 m, and a compressive horizontal tectonic stress of  $-6$  MPa (Figure 5). Values of other parameters are listed in Table I. In this reference case, the horizontal compressive stress is concentrated beneath the valley floor and reduced beneath the ridgetops (Figure 5(a)) (Savage and Swolfs, 1986). The differential stress (the difference between  $\sigma_1$  and  $\sigma_3$  in Figure 5(d)) and the potential for shear failure, as measured by  $C_{min}$  (Figure 5(e)), are therefore much larger beneath the valley than beneath the ridges. For modest rock cohesion of 1 MPa and unconfined compressive strength  $q_u = 3$  MPa, the zone of fracturing (opening mode at the surface, shear mode at depth) is restricted to a crescent-shaped zone beneath the valley (Figure 5(f)).

We repeated these calculations for different model parameters and topographic profiles to examine the sensitivity of the results in Figure 5 to ambient stress, rock properties, and

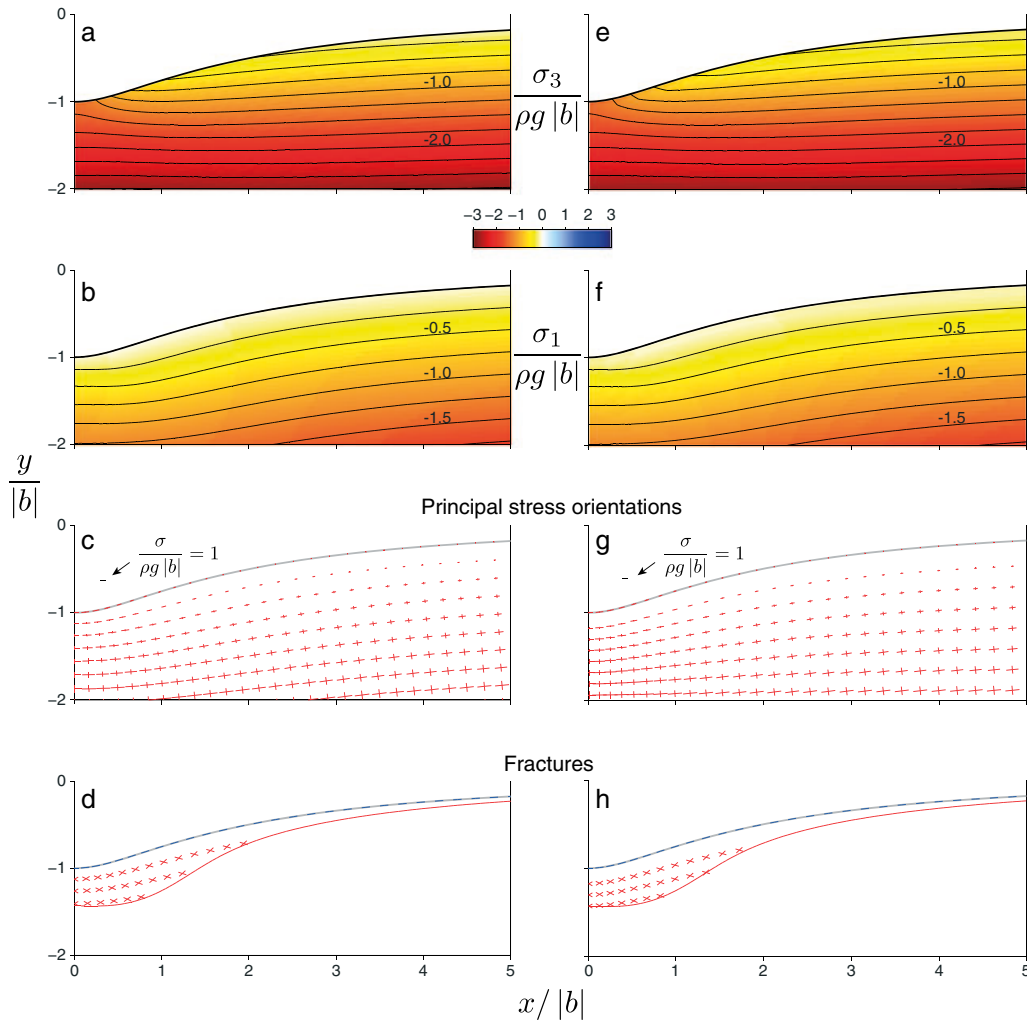
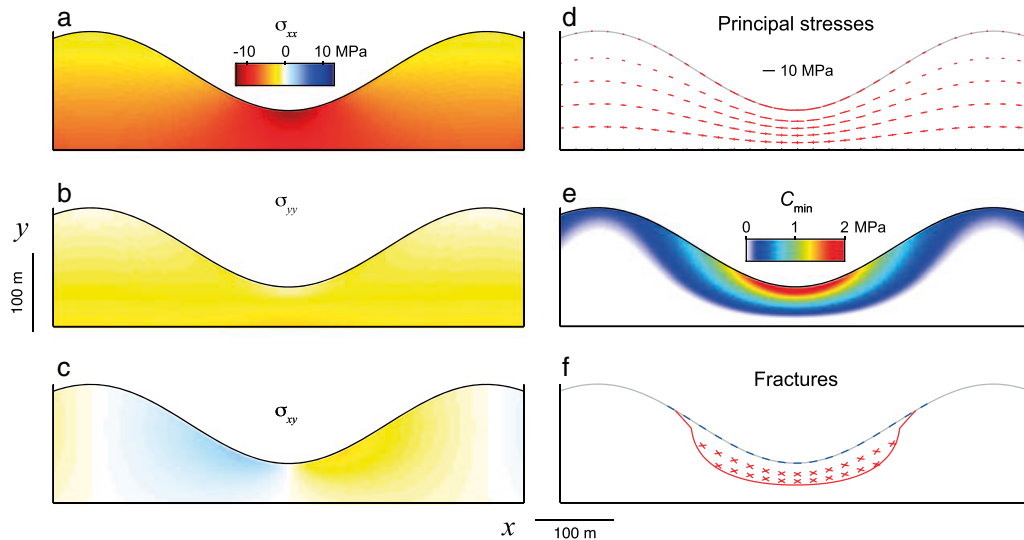


**Figure 4.** Comparison of principal stresses and fracture patterns in boundary element model solutions (e)–(h) with analytical solutions of Miller and Dunne (1996) (a)–(d) for the ‘high regional compression’ scenarios shown in their Figures 4 and 7. Despite the description, this scenario has an ambient horizontal surface stress of  $\sigma_{xx}^{a,0} = 0$ . The symmetric valley topography (only half of which is shown) is defined by the conformal coordinate mapping of Savage *et al.* (1985) with  $a = 2.5$  and  $b = -1$ . Other parameter values are listed in Table I. Coordinates and stresses are normalized as indicated. Contours in (a), (b), (e) and (f) are stresses in the same units as the color scale. Orientations and lengths of line segments in (c) and (g) show orientations and magnitudes of principal stresses, with red segments indicating compression. In (d) and (h), blue line segments indicate potential opening-mode fractures and red line segments indicate potential shear fractures. Locations of stress and fracture symbols differ between the analytical and numerical solutions because symbols in (c, d) follow the conformal coordinate mapping whereas symbols in (g, h) are located at gridded BEM observation points. This figure is available in colour online at [wileyonlinelibrary.com/journal/espl](http://wileyonlinelibrary.com/journal/espl)

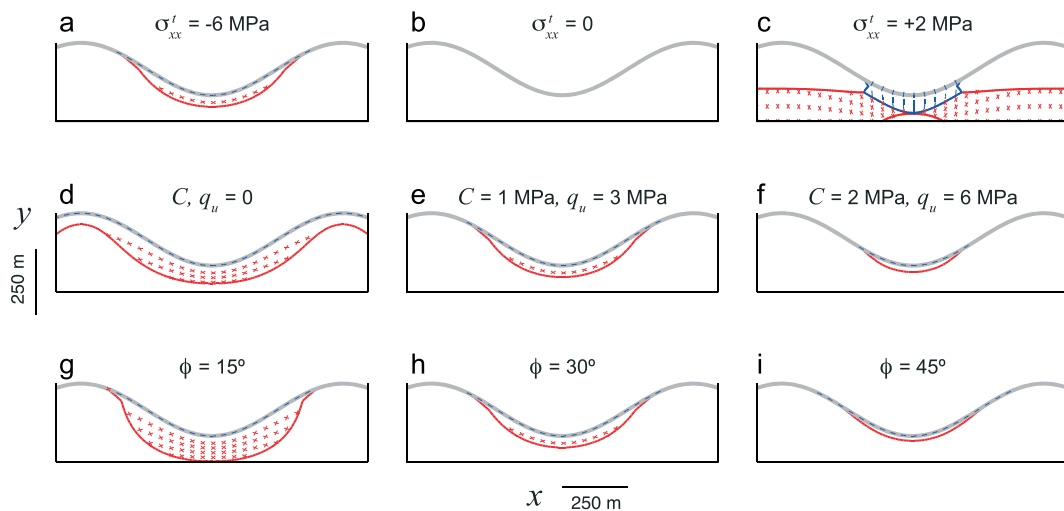
topography. Figure 6 shows how calculated regions of rock failure respond to variations in ambient stress and rock properties. Ambient tectonic stress has a strong effect on the occurrence and mode of predicted fractures. In the presence of gravity but the absence of horizontal tectonic compression, the topography alone is insufficient to fracture rock with modest  $C$  and  $q_u$  (Figure 6(b)). If the horizontal tectonic stress becomes tensile, shear fractures are predicted at depth, and a shallow zone of steeply dipping opening-mode fractures is predicted beneath the valley (Figure 6(c)). For the reference case with a compressive horizontal tectonic stress of  $-6$  MPa, increasing  $C_{\min}$  and  $q_u$  restricts the opening-mode fractures to a progressively smaller section of the valley floor and the shear fractures to a progressively narrower and shallower zone beneath the valley floor (Figure 6(d)–(f)). These trends can be understood by examining the magnitudes of the surface-parallel principal stress (Figure 5(d)) and  $C_{\min}$  (Figure 5(e)), respectively. Finally, increasing the internal friction angle restricts shear failure to a shallower and horizontally narrower zone beneath the valley (Figure 6(g)–(i)). This trend occurs because a larger friction angle, which corresponds to a steeper failure envelope (Figure 3), allows rock to withstand a larger differential stress without fracturing.

Figure 7 shows how the predicted region of rock failure depends on the relief, shape and asymmetry of the topographic profile. Higher relief (for a fixed wavelength) deepens the zone of shear fractures on either side of the valley axis (Figure 7(a)–(c)). Sharp ridges (Figure 7(f)) have little effect on the valley-centered fracture patterns in the reference case examined here, but a sharp valley (Figure 7(d)) reduces the depth of the shear fracture zone to zero at the valley axis and deepens it elsewhere, creating two lobate zones on either side of the valley. Asymmetry of hillslope relief (Figure 7(g)) or hillslope length (Figure 7(i)) makes the predicted regions of rock failure asymmetric.

These calculations for synthetic topography illustrate three general trends. First, tectonic compression favors shear fracture in the subsurface based on laboratory fracture criteria. Although Miller and Dunne (1996) emphasized the potential for opening-mode fracture beneath ridges and valleys, this result was partly a consequence of the absence of a constant horizontal compression term in their ambient stress field ( $\sigma_{xx}^t = 0$  in Equation 1a). For topographic scenarios like those in Figures 5–7, we find that modest regional compression ( $\sigma_{xx}^t < 0$ ) inhibits the formation of tensile fractures in the subsurface. (This result is limited to



**Figure 5.** Boundary element model solution for stresses ((a)–(d)), the minimum cohesion to prevent shear fracture,  $C_{\min}$  (e), and fracture modes and orientations (f) beneath a sinusoidal topographic profile subjected to a compressive ambient horizontal stress of  $-6$  MPa. See Table I for other parameters. The entire topographic profile used in the calculation extends several wavelengths beyond the portion shown, and tapers to a level surface at the ends. Color scale in (a) applies to (a), (b), and (c). Orientations and lengths of line segments in (d) show orientations and magnitudes of principal stresses, with red segments indicating compression. In (f), blue line segments indicate potential opening-mode fractures and red line segments indicate potential shear fractures. This figure is available in colour online at [wileyonlinelibrary.com/journal/espl](http://wileyonlinelibrary.com/journal/espl)



**Figure 6.** Boundary element model solutions showing the sensitivity of the predicted rock fracture regions to variations in ambient horizontal tectonic stress ((a)–(c)), rock strength ((d)–(f)), and rock friction angle ((g)–(i)). Panels (a), (e), and (h) use the same parameters as Figure 5. Parameters for other panels are the same as in Figure 5 except where indicated, and except  $\Delta x = 10$  m (see Table I). Gray line is the land surface. Blue line segments indicate opening-mode fractures and red line segments indicate shear fractures. Red lines mark the boundaries of the zones where shear fractures are predicted; where no upper boundary is indicated, shear fractures are predicted up to, but not including, the land surface. Blue line in (c) marks the boundary of the zone where opening mode fractures in tension are predicted; in panels (a) and ((d)–(i)), opening mode fractures are predicted only at the land surface, where the rock is in unconfined compression. This figure is available in colour online at [wileyonlinelibrary.com/journal/espl](http://wileyonlinelibrary.com/journal/espl)

‘modest’ compression because large surface-parallel compressive stresses can cause surface-parallel tensile fractures to form beneath ridges (Martel, 2006, 2011). Second, in a compressive tectonic regime ( $\sigma'_{xx} < 0$ ), the greatest susceptibility to shear fracture occurs in a zone beneath the valley floor, which extends deeper for larger tectonic compression, lower rock cohesion, or a smaller rock friction angle (Figure 6). Third, the shape of this zone of shear fracture is most sensitive to the sharpness of the ‘V’ formed by the valley side slopes (Figure 7(d)), and less sensitive to the ridgeline shape, valley relief, and valley asymmetry. In the next section, we use these observations to guide our analysis of a field site with a more irregular topographic profile.

## Application to the Shale Hills, Pennsylvania, USA

The ability to calculate stresses beneath an irregular topographic profile permits direct comparisons of modeled stresses with observed rock damage at real field sites with irregular topography. An exhaustive comparison is beyond the scope of this study; instead, we offer a comparison that demonstrates the potential for future investigations. We sought a site with uniform rock type in a region where the tectonic stress field is reasonably well constrained; with a valley extending roughly perpendicular to the maximum horizontal stress, such that a



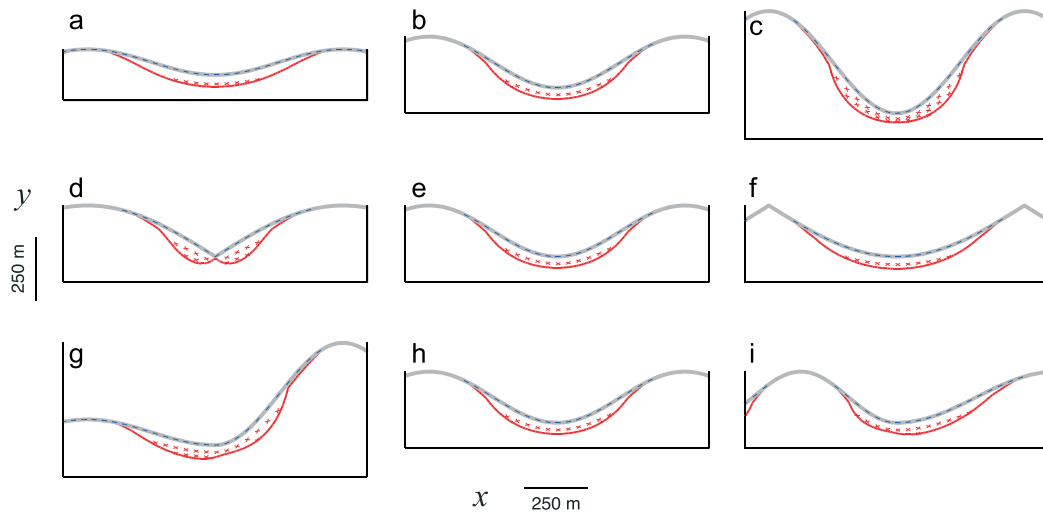


**Figure 7.** Boundary element model solutions showing the sensitivity of predicted fracture patterns to variations in relief ((a)–(c)), valley and ridge shape ((d)–(f)), and asymmetry in valley relief (g) and width (i). Model parameters are the same as in Figure 5, except  $\Delta x = 10$  m (see Table I). Panels (b), (e), and (h) have the same profile shape as Figure 5. Far-field topography (not shown) and symbols are the same as in Figure 6. This figure is available in colour online at [wileyonlinelibrary.com/journal/espl](http://wileyonlinelibrary.com/journal/espl)

plane strain approximation can reasonably be applied along a valley cross-section; where a high-resolution topographic survey has been performed, and where bedrock fractures have been imaged at depths comparable with the topographic relief. Few sites satisfy all these criteria and offer extensive opportunities to observe subsurface rock damage. However, an established study site in Pennsylvania, USA, has all of these characteristics and is suitable for a preliminary investigation.

### Site description

The Susquehanna Shale Hills Critical Zone Observatory (hereafter referred to as the Shale Hills or SSHO) is a  $0.08 \text{ km}^2$  catchment located in the Shaver's Creek drainage basin in the uplands of the Valley and Ridge physiographic province of central Pennsylvania, USA (Figure 8). The forested, soil-mantled valley has an average local relief (valley floor to ridgetop) of 20 m, side slopes with gradients of 25–35%, and a stream with an average channel gradient of 4.5% that flows west-southwest in its headwaters and northwest near the basin outlet. The catchment is eroded into the Silurian Rose Hill Formation of the Clinton Group, which consists of shale with minor interbedded limestones of variable thickness (Jin *et al.*, 2010). Although the area is currently tectonically inactive, the bedrock has experienced a long history of deformation associated with the ancient orogenic events that formed the Valley and Ridge. Outcrops of shale beds on the valley floor have an average strike of S54°W and an average dip of N76°W (Jin *et al.*, 2010), but much shallower bedding dips of approximately 30° are observed in borehole image logs (Kuntz *et al.*, 2011).

The SSHO site meets several key criteria listed above. Aside from local structural differences, the shale bedrock is relatively uniform. Near the outlet of the valley, where the stream flows northwest, the valley axis is roughly perpendicular the maximum regional horizontal stress, as described below. The site's topography has been surveyed with high-resolution airborne laser altimetry through the State of Pennsylvania's PAMAP program and by the National Center for Airborne Laser Mapping (NCALM). Finally, optical image logs from a set of boreholes located at the downstream end of the valley permit detailed observations of fractures (Kuntz *et al.*, 2011).

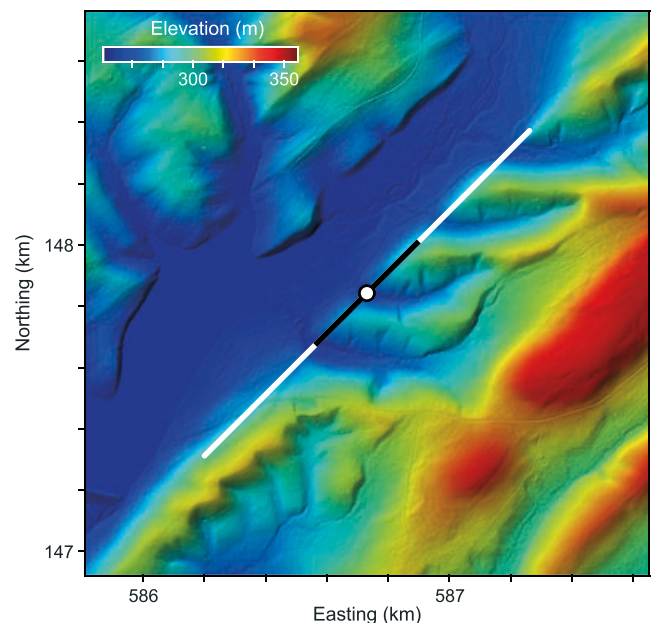


**Figure 8.** Shaded relief map of the Shale Hills study site and surrounding area showing location of boreholes (white circle), the transect used in model calculations (white line), and the portion of the transect shown in Figures 10 and 11. Pennsylvania South State Plane projection (zone 3702), NAD83 datum. Topographic data from the 1/9 arcsecond US National Elevation Dataset. See Figure 9 for the location of the site within the state of Pennsylvania. This figure is available in colour online at [wileyonlinelibrary.com/journal/espl](http://wileyonlinelibrary.com/journal/espl)

### Regional tectonic stress

We used measurements compiled in the World Stress Map database (Heidbach *et al.*, 2008) to estimate the orientation and magnitude of the ambient horizontal tectonic stress,  $\sigma_{xx}^t$ . A compilation of earthquake focal mechanisms, borehole break-outs, overcoring measurements, hydrofracture events, and geologic features indicates that the horizontal stresses in the region are compressive and that the most compressive horizontal stress is oriented roughly northeast–southwest (Figure 9). Most of the observations in the database only include a direction, but a small number include a horizontal stress magnitude and

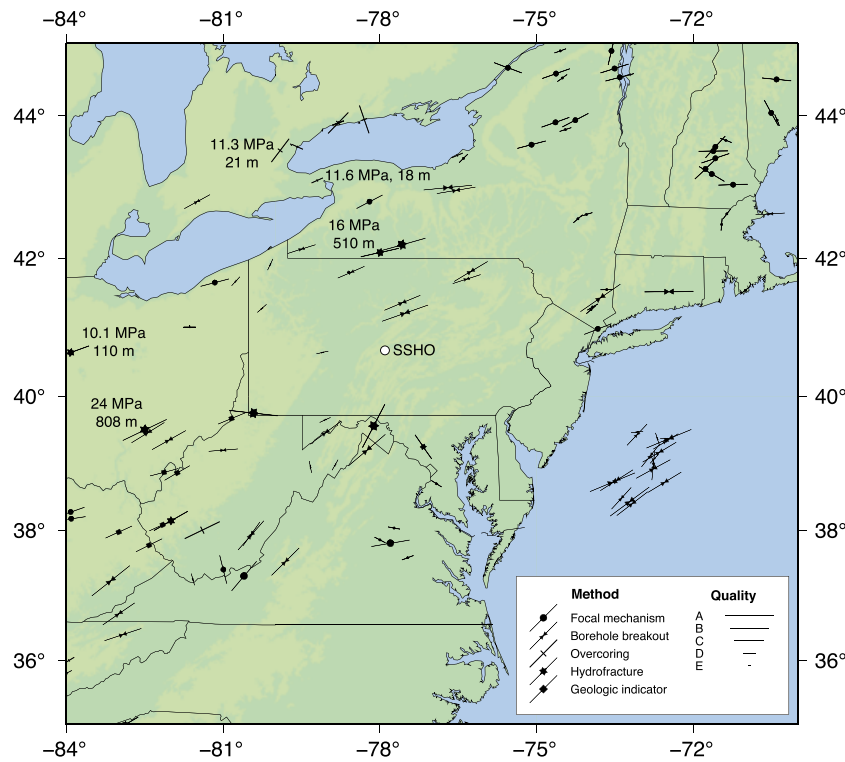


**Figure 9.** Map of orientations of maximum horizontal crustal stress measurements, modified from the World Stress Map (Heidbach *et al.*, 2008). Symbols indicate the method used to estimate the stress orientation, and size and length of the symbols correspond to a qualitative measure of the quality of the measurement (see key). Magnitudes and depths of measurements are labeled where magnitude estimates were reported in the literature. Table II lists estimates of the maximum and minimum horizontal stresses at the surface based on these reported values, as well as the original references. The location of the SSHO field site is marked with a white circle. This figure is available in colour online at [wileyonlinelibrary.com/journal/espl](http://wileyonlinelibrary.com/journal/espl)

the depth at which it was measured. These observations are marked in Figure 9 and listed in Table II.

To convert the horizontal stress estimates at depth,  $\sigma_h$ , to horizontal surface stress,  $\sigma_h^0$ , we assumed that the depth variation in stress magnitude is entirely due to overburden, such that

$$\sigma_h = \sigma_h^0 + \rho g d \frac{\nu}{1 - \nu} \quad (10)$$

where  $d$  is depth beneath the surface and  $\nu$  is Poisson's ratio. We solved Equation (10) for  $\sigma_h^0$  and used  $\rho = 2650 \text{ kg/m}^3$ . Table II lists the resulting estimates of maximum and minimum horizontal stress for  $\nu = 1/4$  and  $\nu = 1/3$ . Maximum and minimum horizontal surface stresses are both compressive for all sites in Table II, with the maximum compressive stress typically about twice the magnitude of the minimum stress. The means and standard deviations for  $\nu = 1/3$  are  $\sigma_{h,\max}^0 = -10.8 \pm 1.9 \text{ MPa}$

and  $\sigma_{h,\min} = -5.0 \pm 2.1 \text{ MPa}$ , and the estimates for  $\nu = 1/4$  are slightly larger. In subsequent calculations for the SSHO, we use a conservative estimate of  $\sigma_{xx}^t = -10 \text{ MPa}$ , with the  $x$  direction in the model approximately aligned with the direction of the most compressive horizontal stress.

### Modeled stress and fracture patterns

We used the PAMAP laser altimetry data to extract a topographic profile along a 1.5 km transect oriented  $45^\circ$  east of north, which is perpendicular to the valley axis at the location of the boreholes (Figure 8) and nearly parallel to the orientation of the most compressive regional horizontal stress (Table II, Figure 9). The transect passes through one of the boreholes, CZMW 1 (Kuntz *et al.*, 2011), and within 10 m of the other three boreholes. Because the boreholes are located near the

**Table II.** Regional stress estimates. All stresses in MPa

| WSM ISO*                  | Lat, Lon        | Azimuth | Depth (m) | $\sigma_{h,\max}$ | $\sigma_{h,\min}$ | $\nu = 1/4$         |                     | $\nu = 1/3$         |                     |
|---------------------------|-----------------|---------|-----------|-------------------|-------------------|---------------------|---------------------|---------------------|---------------------|
|                           |                 |         |           |                   |                   | $\sigma_{h,\max}^0$ | $\sigma_{h,\min}^0$ | $\sigma_{h,\max}^0$ | $\sigma_{h,\min}^0$ |
| CAN336 <sup>oc,1</sup>    | 43.10°, -79.20° | 66°     | 18        | -11.6             | -8.3              | -11.4               | -8.1                | -11.4               | -8.0                |
| CAN337 <sup>oc,2</sup>    | 43.90°, -78.80° | 68°     | 21        | -11.3             | -6.6              | -11.1               | -6.4                | -11.0               | -6.4                |
| USA926 <sup>hf,3,4</sup>  | 42.08°, -78.00° | 77°     | 510       | -16               | -10.1             | -11.6               | -5.7                | -9.4                | -3.5                |
| USA58 <sup>hf,3,4,5</sup> | 39.50°, -82.50° | 64°     | 808       | -24               | -14               | -17.0               | -7.0                | -13.5               | -3.5                |
| USA939 <sup>hf,4,6</sup>  | 40.64°, -83.92° | 70°     | 110       | -10.1             | -5.1              | -9.1                | -4.1                | -8.7                | -3.7                |
|                           |                 |         |           | Mean              |                   | -12.1               | -6.3                | -10.8               | -5.0                |
|                           |                 |         |           | s.d.              |                   | 2.9                 | 1.5                 | 1.9                 | 2.1                 |

\*World Stress Map identification code (Heidbach *et al.*, 2008). Techniques: <sup>oc</sup>= overcoring, <sup>hf</sup>= hydrofracture. References: <sup>1</sup>Palmer and Lo (1976), <sup>2</sup>Lo (1981a,1981b), <sup>3</sup>Haimson (1974), <sup>4</sup>Haimson and Doe (1983), <sup>5</sup>Overbey and Rough (1968), <sup>6</sup>Haimson (1983).

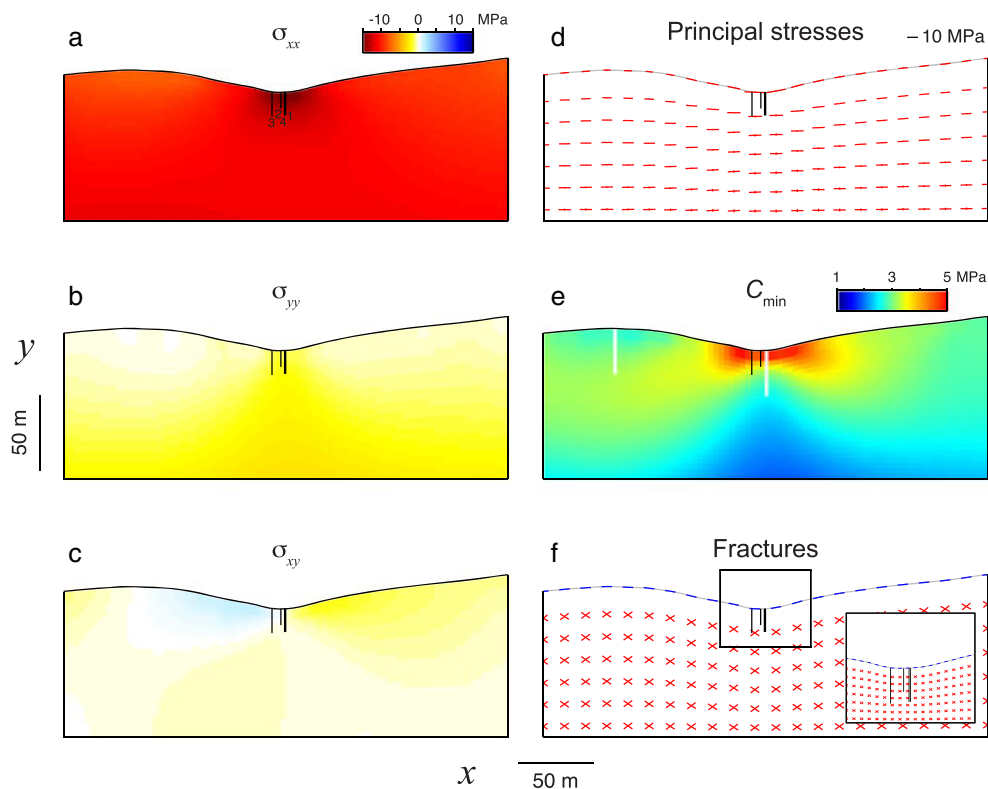
basin outlet, the extracted profile has somewhat lower relief than the middle part of the valley. The three-dimensional shape of the valley (curved valley axis, longitudinal slope, downstream variations in relief) undoubtedly produces some three-dimensional stress variations, but given the elongated valley shape and relatively gentle longitudinal profile, we assume that the three-dimensional effects are small relative to the topographic stresses generated by the valley cross-sectional shape and that a two-dimensional treatment of the state of stress is a reasonable approximation. We subtracted the mean elevation from the profile and tapered the ends of the profile to an elevation of zero with a Tukey (tapered cosine) window. This tapering of the endpoints to a common elevation, which is performed to ensure a stress equilibrium in the model calculation, only affects the topography far from the Shale Hills catchment (Figure 8).

The topographic profile was resampled by linear interpolation to a horizontal point spacing of  $\Delta x = 3.5$  m, and the resampled points were used as the endpoints of the boundary elements. We then defined a mesh of subsurface observation points with  $x$  locations centered beneath element midpoints and spanning 150 m on either side of the valley axis. A uniform number of  $y$  locations are chosen beneath each element midpoint, with the  $y$  locations below a particular element midpoint being spaced at equal intervals from one element length below the surface to a depth of 100 m below the ends of the tapered profile. The depth intervals of the observation points therefore vary along the profile, as shown schematically in Figure 1.

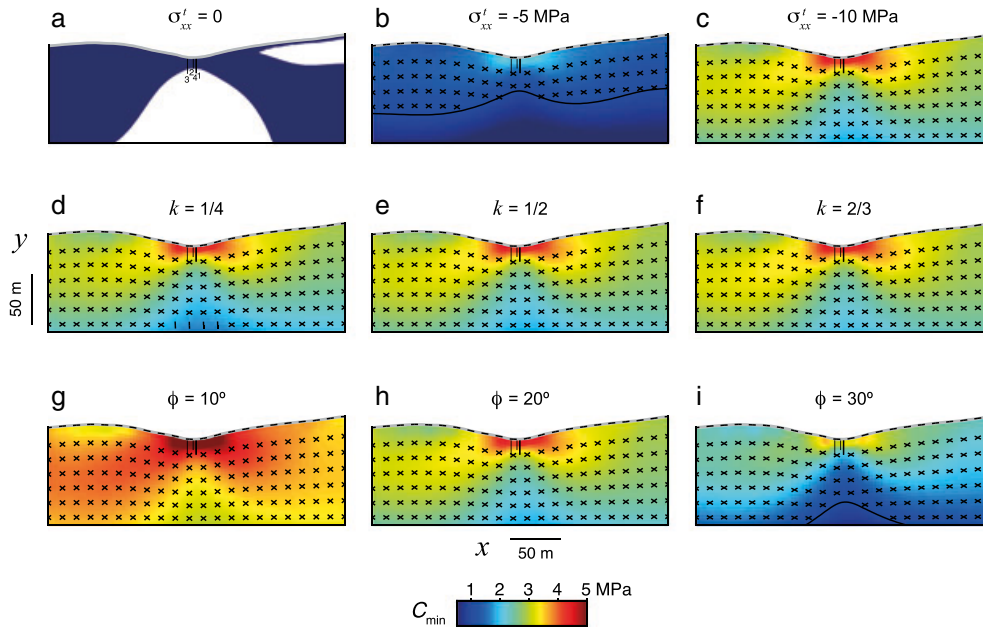
We used the boundary element model to calculate stresses beneath the SSHO topographic profile in the presence of a  $-10$  MPa ambient horizontal tectonic stress, using typical parameters for shales in the region (Table I; Goodman, 1989).

Figure 10 shows horizontal and vertical normal stresses, vertical shear stresses, principal stress orientations and magnitudes, the shear fracture proxy  $C_{\min}$ , and predicted fracture modes and orientations. Horizontal normal stresses ( $\sigma_{xx}$ ) are compressive throughout the landscape, but are least compressive under the ridgetops and most compressive under the valley floor (Figure 10(a)). Vertical normal stresses ( $\sigma_{yy}$ ) follow a similar pattern (Figure 10(b)). The most compressive stress trajectories are horizontal or nearly so, forming a pattern that resembles a subdued version of the topographic surface (Figure 10(d)). The topographic effect on the shear fracture proxy,  $C_{\min}$ , is pronounced (Figure 10(e)). The location most susceptible to shear fracturing is a shallow zone extending approximately 10 m beneath the valley floor, where rocks with a cohesion less than about 5 MPa are expected to fail.  $C_{\min}$  declines rapidly with depth beneath this shallow zone. Beneath the ridges,  $C_{\min}$  increases slightly with depth down to a depth of a few tens of meters, and then declines gradually at greater depths. Rock with cohesion less than about 2 MPa is expected to fracture in shear at all subsurface locations shown in the figure (Figure 10(f)). The only location where opening mode fractures are predicted by the criteria of Miller and Dunne (1996) is at the land surface, where the rocks are unconfined and subject to surface-parallel compression (Figure 10(d), (f)).

We examined the sensitivity of these stress and predicted fracture patterns to the ambient tectonic stress and rock mechanical parameters by repeating the calculation in Figure 10 for different values of  $\sigma_{xx}^t$ ,  $k$ , and  $\phi$ . Figure 11 shows the effects on  $C_{\min}$  and fracture patterns when each of these parameters deviates from the value used in Figure 10. Variations in ambient tectonic stress have a strong effect: halving  $\sigma_{xx}^t$  from  $-10$  MPa (Figure 11(c)) to  $-5$  MPa (Figure 11(b)) reduces  $C_{\min}$  and causes



**Figure 10.** Boundary element model solution for stresses ((a)–(d)),  $C_{\min}$  (e), and fracture modes and orientations (f) beneath the Shale Hills transect in Figure 8 for a compressive ambient horizontal surface stress of  $-10$  MPa (Figure 9, Table II). See Table I for other parameters. Locations of wells are indicated, and well numbers are labeled in (a). Red line segments in (d) indicate compression. Vertical white lines in (e) indicate the locations of vertical profiles plotted in Figure 15(a), (b). In (f), blue line segments indicate opening mode fractures at the land surface, and red line segments indicate shear fractures. Inset shows a solution in the vicinity of the wells with higher spatial resolution. Color scale in (a) applies to (a), (b), and (c). This figure is available in colour online at [wileyonlinelibrary.com/journal/espl](http://wileyonlinelibrary.com/journal/espl)



**Figure 11.** Boundary element model solutions showing the sensitivity of the calculated  $C_{min}$  values and fracture patterns in Figure 10 to variations in ambient horizontal tectonic stress ((a)–(c)), the ratio of the depth gradient of horizontal stress to the depth gradient of vertical stress ((d)–(f)), and rock friction angle ((g)–(i)). Panels (c), (e), and (h) are the same scenario as Figure 10. Parameters for other panels are the same as in Figure 10 except where indicated (see Table I). Gray line is the land surface. Crossing black line segments below the surface represent shear fractures, and single black line segments at the surface represent opening mode fractures. Single near-vertical black segments at the lower edge of (d) represent shear fractures associated with an out-of-plane least compressive principal stress, in which case both shear fracture planes intersect the plane of the cross-section along the same line. Solid black curves in (b) and (i) mark the lower boundaries of the zones where shear fractures are predicted for the specified cohesion of 1 MPa; in all panels except (a), shear fractures are predicted up to, but not including, the land surface. Locations of wells are indicated, and well numbers are labeled in (a). Color plots in the background show  $C_{min}$ , the minimum cohesion required to prevent shear fracturing. This figure is available in colour online at [wileyonlinelibrary.com/journal/espl](http://wileyonlinelibrary.com/journal/espl)

predicted shear fractures to be confined to a zone that is shallower beneath the valley than beneath the ridges. In the absence of tectonic stress, the topography alone is not enough to cause shear fractures in two areas (white areas in Figure 11(a)): (1) a zone that begins about 10 m below the valley floor and broadens at greater depths, and (2) a zone beneath the higher ridge on the northeast side of the valley. Even outside these zones, rock cohesion exceeding about 1 MPa will prevent fractures from forming (Figure 11(a)). Variations in  $k$  have a weak effect, with smaller values generating a somewhat steeper decline in  $C_{min}$  beneath the valley floor (Figure 11(d)–(f)). As the internal friction angle increases, predicted shear fractures take on shallower dips and the magnitude of  $C_{min}$  declines, indicating a lower potential for shear fracture, but the relative spatial pattern of  $C_{min}$  is largely unchanged (Figure 11(g)–(i)). These sensitivity tests show that the most robust features of the modeled stress and fracture patterns are the relative differences in the potential for shear fracturing (as expressed by  $C_{min}$ ) beneath ridges and valleys and the trends in  $C_{min}$  with increasing depth. We therefore focus our observational comparisons on these features.

## Borehole fracture mapping

To produce an observational dataset for comparison with the stress and fracture calculations, we mapped fractures in optical images of the four boreholes in the valley bottom. Image logs of the borehole walls, such as the example in Figure 12, were acquired with an optical borehole imaging (OBI) televiewer manufactured by Mount Sopris Instruments. The OBI produces a vertically continuous, 360° image of the borehole wall using a charge-coupled device (CCD) camera and uses a 3-axis magnetometer and two accelerometers to measure the compass

orientation of the image and deviation of the borehole from vertical. Resolution of the images was approximately 0.5 mm vertically and 0.33 mm azimuthally, though image noise typically created a coarser effective resolution. The image logs were processed, oriented to magnetic north and analyzed with WellCAD, a PC-based software package. No deviation corrections were made, as the wells are vertical. The wells are cased with polyvinyl chloride (PVC) pipes from the ground surface to a depth of 3 m, so fractures could not be mapped in this shallow zone. No casing exists below that depth, obviating the need for casing-effect corrections of the images.

The main structures visible in the borehole image logs are natural fractures and bedding planes. Neither drilling-induced fractures nor borehole breakouts are apparent in the images. Planar features that intersect a cylindrical borehole wall have sinusoidal traces on the flattened image logs (Figure 12). The phase angle of a sinusoidal trace relative to a reference mark yields the strike of the plane, and the trace amplitude yields the dip (Serra, 1989; Luthi, 2001). In the SSHO boreholes, bedding planes have consistent attitudes at a given depth and parallel planar changes in rock color, whereas fractures commonly crosscut bedding planes (Figure 12). We used rock color and cross-cutting relationships to classify each planar feature as a bedding plane or a fracture (Figure 13). We generally could not identify offsets along fractures. Each feature was traced eight times (by mapping all features, recording the sinusoidal traces, deleting the traces, and starting again), and the strike and dip of a feature were recorded as the arithmetic averages of the eight strike directions and dip angles. Strike and dip orientations were corrected for magnetic declination to yield orientations relative to geographic north.

Stereonet plots of the poles to fracture and bedding planes (Figure 14) show generally consistent orientations in all four boreholes, as expected for boreholes within about 12 m of



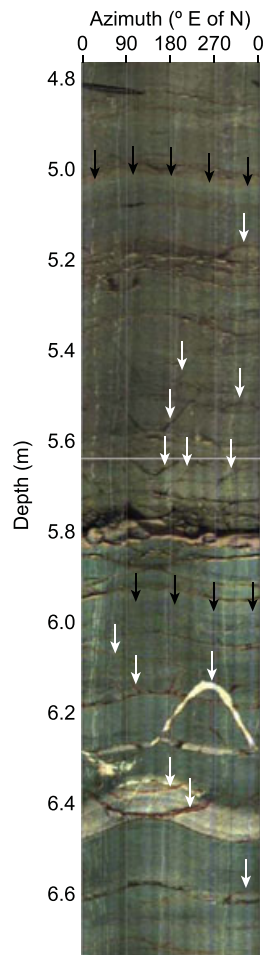


**Figure 12.** Example section of borehole image log from well 1. Black arrows mark examples of color differences used to identify bedding planes. White arrows mark examples of fractures. Planar features that intersect the borehole have sinusoidal traces in this unwrapped view of the borehole walls. Image orientations are relative to magnetic north. This figure is available in colour online at [wileyonlinelibrary.com/journal/espl](http://wileyonlinelibrary.com/journal/espl)

one another. Fractures generally dip steeply to the NNW or SSE, except for a few fractures that dip steeply E or W (Figure 14(a)), whereas bedding is either approximately horizontal or dips gently to the NNW. The gentle bedding dips contrast with the report of Jin *et al.* (2010) but agree with our observations of outcrops as well as those of Kuntz *et al.* (2011).

## Comparison of fractures with modeled topographic stresses

### Fracture orientation

The observation that most fractures in the boreholes dip steeply to the NNW or SSE (Figure 14(a)) suggests that they may be conjugate sets of shear fractures. However, these fractures are approximately orthogonal to the expected NE or SW dip directions of shear fractures triggered by stresses along the cross-valley SSHO transect (Figure 8). One possible explanation for this difference in orientation is that the observed fractures were caused by topographic stresses, but the three-dimensional effects of the topography near the outlet of the SSHO valley caused the stress field to deviate from the plane strain conditions assumed in our model calculation. Another possible explanation is that the fractures are older features that may (or may not) have experienced renewed sliding under the influence of recent topographic and tectonic stress. The fact that both fractures (Figure 14(a)) and dipping bedding planes (Figure 14(b)) strike in approximately the

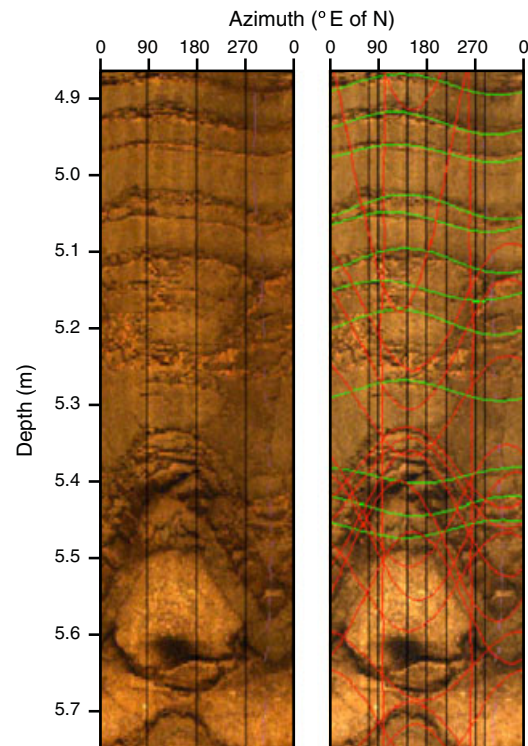


**Figure 13.** Section of a borehole image log from well 4. Left image shows untraced bedding and fracture planes. Right image shows the same section of the borehole wall with structural features traced. Green low-amplitude traces indicate gently dipping bedding planes, and red high-amplitude traces indicate steeply dipping fracture planes. Image orientations are relative to magnetic north. This figure is available in colour online at [wileyonlinelibrary.com/journal/espl](http://wileyonlinelibrary.com/journal/espl)

same direction as regional valley and ridge structural features (Figure 8) supports the latter explanation.

Either scenario makes it difficult to test the topographic fracture hypothesis by comparing observed fracture orientations with a two-dimensional stress model. But in both scenarios, the presence of the SSHO valley should still perturb the stress field and alter the potential for rock damage beneath ridges and valleys. We therefore turn to a more general measure of spatial variations in rock damage that may have been influenced by topography: trends in fracture abundance with depth beneath the surface.

### Fracture abundance

We seek a measure of the intensity of fracturing that is also relevant to near-surface hydrologic and geomorphic processes. One simple proxy is the number of fractures per unit distance along a linear path through the rock, which we refer to as the linear fracture abundance. Fractures that intersect a linear path and are highly inclined with respect to that path appear to be spaced farther apart than fractures that are more nearly perpendicular to the path (Terzaghi, 1965; Martel, 1999). Steeply dipping fractures are therefore likely to be under-represented in our vertical boreholes. We accounted for this bias by calculating a weighted linear fracture abundance. We divided each borehole into five equal depth intervals and binned the fractures according to the depth at which the fracture plane intersects the borehole axis. Each fracture was assigned a weight equal to  $1/\cos \psi$ , where  $\psi$  is the fracture's dip angle (Terzaghi, 1965; Martel, 1999). The weighted linear fracture abundance is the sum of the weights in each bin divided by the vertical length of the bin. Linear fracture abundance declines steeply with depth in all four SSHO boreholes, ranging from approximately 30 fractures per meter at a depth of 3 m (the bottom of the borehole casing) to fewer than two fractures per meter at a depth of 15 m (Figure 15(c)).

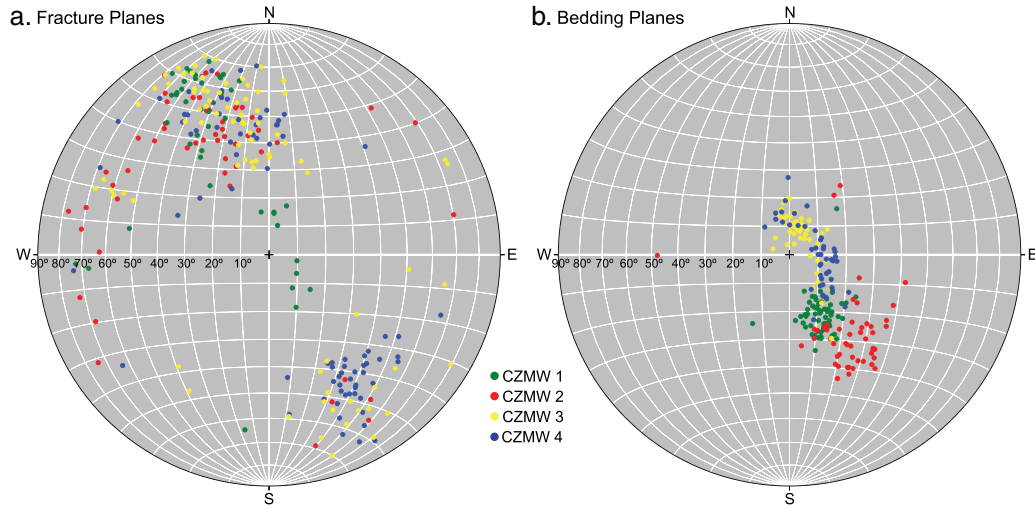


**Figure 14.** Stereonets showing measured orientations of poles to (a) fractures and (b) bedding planes in the wells. Points are the intersections of the poles to the planes with the lower hemisphere, such that steeper-dipping planes plot closer to the outer circle. Dip angles for planar features corresponding to the poles are indicated on the grid. Orientations are relative to geographic north. This figure is available in colour online at [wileyonlinelibrary.com/journal/espl](http://wileyonlinelibrary.com/journal/espl)

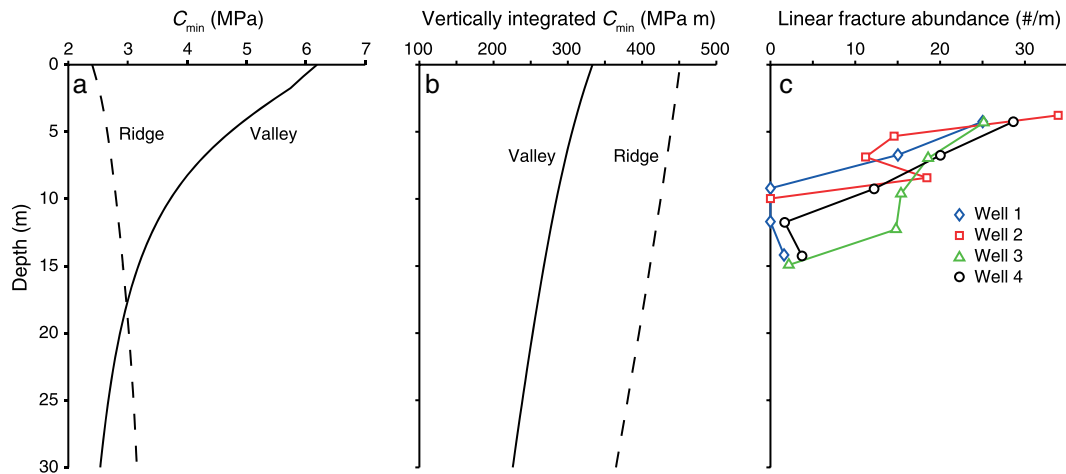


**Figure 15.** Comparison of measured fracture abundance with model-based proxies for shear fracture. (a) Depth profiles of  $C_{\min}$  beneath the valley floor and ridgetop at the locations indicated in Figure 10(e). (b) Depth profiles of vertically integrated  $C_{\min}$  at the same locations. (c) Depth profiles of weighted linear fracture abundance beneath the valley floor, based on fracture counts in borehole image logs. The gap in fracture abundance near the surface occurs because the wells are cased from the surface to 3 m depth, so no fractures could be measured in that depth range. This figure is available in colour online at [wileyonlinelibrary.com/journal/espl](http://wileyonlinelibrary.com/journal/espl)

These observed trends in fracture abundance can be compared with  $C_{\min}$ , the shear fracture proxy (Figure 10(e)). The specific quantity to be compared with fracture abundance depends on how fractures accumulate as rock is exhumed toward the land surface. If fractures only form close to the surface, or if fractures heal rapidly (through recrystallization or secondary mineral deposition, for example) relative to the rate of exhumation, the abundance of active fractures at a given location in the subsurface should be most influenced by the present-day stress state, and the most appropriate quantity to compare would be the local value of  $C_{\min}$ . If fractures form over a range of depths and times and never heal, then the abundance of active fractures at a given location in the subsurface will reflect the cumulative effects of the different stress states the rock experienced on its way to its present location. In this case, a more appropriate proxy to compare would be the integrated  $C_{\min}$  between the depth at which the rock began to accumulate fractures and its present depth. (This assumes that the topography and tectonic stress have not changed as the rock was exhumed, an idea we return to in the Discussion.) We calculate the vertically integrated value of  $C_{\min}$  at a depth  $z$  as

$$\int_{z_0}^z C_{\min}(z') dz' \quad (11)$$

where  $z_0$  is the depth at which the rock begins to accumulate fractures, here taken to be the depth at which  $C_{\min} = 1$  MPa (approximately 200 m for the scenario in Figure 10(e)). The actual history of fracture accumulation may lie between these two end-member cases.

Figure 15 compares the observed depth profiles of fracture abundance beneath the valley bottom (Figure 15(c)) with the present-day depth profile of  $C_{\min}$  (Figure 15(a)) and the vertically integrated  $C_{\min}$  (Figure 15(b)). For comparison, we also plot in Figures 15(a) and 15(b) the predicted trends beneath the highest ridgetop, where the vertical trends in  $C_{\min}$  differ most from those beneath the valley floor (Figure 11(e)).  $C_{\min}$  declines rapidly with depth in the uppermost 15 m beneath the valley floor, then declines more gradually at greater depths (Figure 15(a)). This differs from the vertically integrated  $C_{\min}$  values, which decay more gradually relative to their surface values over the entire depth range shown in Figure 15(b). Under the ridgetop,  $C_{\min}$  increases with depth for the shallow

depths shown in Figure 15(a) (the opposite of the modeled trend beneath the valley), whereas the vertically integrated  $C_{\min}$  declines gradually with depth, similar to the trend under the valley floor but with a larger magnitude (Figure 15(b)). The parameters  $\phi$ ,  $k$  and  $\sigma_{xx}^t$  scale the magnitude of  $C_{\min}$ , but do not have a strong effect on the shapes of these trends (Figure 11). The observed decline in fracture abundance with depth in Figure 15(c) resembles the rapid decline in  $C_{\min}$  more than the gradual decline in vertically integrated  $C_{\min}$ . This suggests that, if the fractures were indeed influenced by topography, the present-day stress field may exert a stronger control on fracture patterns than the stresses experienced by the rocks earlier in their exhumation history. More generally, the similar trends in fracture abundance and  $C_{\min}$  are consistent with the hypothesis that topographic stresses have influenced bedrock fracture patterns at the SSHO site.

Given the distinct trends in  $C_{\min}$  beneath ridges and valleys (Figure 15(a)), a comparison of fracture abundance in boreholes located on ridgetops with those in the valley wells would provide an additional test of the topographic fracture hypothesis. A few ridgetop boreholes exist at the SSHO, but small borehole diameters and fully cased holes prevented us from collecting image logs.

## Discussion

### Testing the topographic fracture hypothesis

The decline in fracture abundance beneath the valley floor at the SSHO site is consistent with the hypothesis that topographic stresses have shaped the distribution of bedrock fractures. However, this trend could have a different origin. With our current dataset, for example, we cannot rule out the possibility that pre-existing fractures are reactivated more frequently near the surface due to the reduced overburden, and that the similar depth trends of fracture abundance and  $C_{\min}$  are only coincidental.

Additional observations would provide a more definitive test of the topographic fracture hypothesis. At the SSHO site, fracture mapping in boreholes located on ridgetops (or other locations along the valley cross-section) would reveal whether the trend of fracture abundance with depth differs beneath ridges and valleys, as predicted by the topographic stress model, or whether the trend is similar throughout the landscape. More broadly, comparisons of modeled stresses and observed fractures at sites with different characteristics from SSHO could provide a test under simpler conditions. Sites with crystalline bedrock containing fewer pre-existing fractures should make topographically influenced fractures stand out more prominently. Higher topographic relief would strengthen the topographic perturbation to the stress field, which should also make any topographic effects on fracture patterns more apparent. Sites with similar lithologic and topographic characteristics but different ambient tectonic stress fields should have different topographically driven fracture patterns, especially if the horizontal tectonic stresses have opposite signs.

### Rock damage and exhumation

If the decline in fracture abundance with depth is a consequence of topographic effects, then its apparent association with the present-day stress field (Figure 15(a)) rather than integrated effects of stresses over depth (Figure 15(b)) merits some discussion. This observation would seem to suggest that fracture patterns beneath the SSHO valley are surprisingly insensitive to the stress history experienced by a parcel of rock during its exhumation. We see at least two possible explanations. First,

rock cohesion may be sufficiently large that the rock only becomes susceptible to topographically influenced fracture when it is very near the surface, within the shallow zone where  $C_{\min}$  is largest (Figure 10(e)). In this scenario, the decline in fracture abundance with depth beneath the valley floor would be a signature of the transition from a shallow zone in which fractures have formed or reactivated, to a deeper zone in which they have not. The second possibility is that fractures formed at depth heal as the rock is exhumed, such that the distribution of active fractures near the surface mainly reflects the local stress field. At sites with relatively slow erosion, such as the Appalachians, fractures might have had enough time to heal as they neared the surface. At typical regional erosion rates of a few tens of meters per million years (Portenga and Bierman, 2011), for example, exhumation through a depth comparable with the SSHO topographic relief would take nearly one million years.

### Stress modeling framework: advantages, limitations, and potential improvements

The analysis presented here demonstrates the potential for comparing stress models with mapped fractures to test for topographic effects on rock damage. The boundary element model calculations of stresses beneath synthetic and natural topography illustrate the advantages of a flexible numerical approach, especially the ability to model the effects of irregular topography and multiple adjacent landforms, and the ability to calculate subsurface stresses only in the area of interest. In addition to modeling the effects of gravity and topography on stresses, the boundary element method can account for the effects of slip on faults (Gomberg and Ellis, 1994; Muller and Martel, 2000; Martel and Langley, 2006; Mitchell, 2010).

Applying the boundary element model to a field site also reveals some limitations that could be removed through improvements to the modeling approach. A two-dimensional stress model may provide a good approximation of the stress field in certain parts of some landscapes, but a three-dimensional model would offer a more flexible and accurate tool for calculating stresses beneath arbitrary topography. All landscapes are really three-dimensional, and even landforms that are nearly two-dimensional may be oriented oblique to regional tectonic stress directions. The displacement discontinuity method of Crouch and Starfield (1983) has been extended to three dimensions (Thomas, 1993; Gomberg and Ellis, 1994), and could be used to calculate topographic stresses with an approach similar to the one presented here. The model employed here considers only elastic stresses. This is reasonable for landforms with relatively low relief, but in other scenarios, such as mountain-scale topography, the effects of plastic deformation on stress relaxation in rock may also be important (Leith *et al.*, 2013a, 2013b).

### Topographic stress and landscape evolution

Fractures are well known to enhance rock erodibility (Molnar *et al.*, 2007), and studies have documented the influence of fractures on the effectiveness of specific erosional processes. Whipple *et al.* (2000) show with a series of field examples that fractures accelerate bedrock river incision by promoting plucking of large blocks of material, whereas relatively unfractured rock appears to erode more gradually through abrasion. Dühnforth *et al.* (2010) showed that glaciers in the Sierra Nevada eroded through more granite during the most recent glacial advance at locations with highly fractured rock than at locations with less fractured rock. Moore *et al.* (2009) found that the retreat rate of bedrock walls above talus slopes



increases exponentially as a composite measure of rock mass strength declines, with joint orientation relative to the rock face exerting the strongest control on retreat rate. These are only a few examples among many. The influence of fractures on rock erodibility prompted Miller and Dunne (1996) and Molnar (2004) to propose hypothetical feedbacks between bedrock fracturing and topography, in which topographic stresses influence the development of bedrock fractures, which in turn alter the evolution of topography by creating spatially variable erodibility. Noting the tendency of valleys to concentrate stresses, they emphasized the possibility of a positive feedback between topographic stresses and valley incision. Leith *et al.* (2013a) present evidence of such a feedback in the form of a deep alpine valley that appears to have developed a pronounced inner gorge as a result of glacial erosion accelerated by topographic stresses. The correlation of topographic stresses and bedrock fracture patterns at the SSHO supports the idea that such feedbacks could occur even in landscapes with relatively low relief.

The stress modeling approach presented here could also provide a flexible framework for modeling co-evolution of topography and stresses. The boundary element model could be combined with an erosional model of landscape evolution to iteratively describe how time-varying stresses and erodibility alter the trajectory of topographic change. A challenging aspect of this problem is that if topography or tectonic stresses change as rock is exhumed, it is necessary to account for the changing stress field by tracking the position and state of damage of a parcel of rock through time as it is advected toward the surface. If fractures heal slowly relative to the rate of exhumation, the population of fractures that reaches the surface will partly reflect the stress effects of prior topographic surfaces. In this scenario, topography, stresses, and fracture patterns could still co-evolve, but the feedbacks could be somewhat damped.

Evaluating possible feedbacks between topographic stresses and landscape evolution will require solutions to other fundamental problems related to bedrock erosion. One challenge is quantifying how rock damage affects erodibility. As rock damage increases, the rock probably erodes more easily (Molnar *et al.*, 2007), but the functional relationship between fracture characteristics and the rate of bedrock erosion is not as clear. A few studies have begun to measure these functional relationships for specific erosion processes in the field (Moore *et al.*, 2009), and valuable clues come from engineering applications such as drilling and dredging (Molnar *et al.*, 2007, and references therein). Molnar *et al.* (2007) also note a distinction between fractures reducing rock strength and fractures transforming rocks into discrete particles small enough to be transported away, both of which influence erodibility.

A second challenge is understanding how the rock beneath an eroding landscape accumulates damage, and whether that damage can heal. We have focused on macroscopic brittle fracture, which is undoubtedly an important type of damage, but others could be significant as well. Citing laboratory experiments that document static fatigue accumulation – time-dependent crack growth in rock samples subject to differential stresses below the macroscopic fracture threshold – Molnar (2004) suggests that modulation of static fatigue by topographic stresses could dominate bedrock damage in eroding landscapes. The lack of a straightforward measure of rock damage or a rate law for damage accumulation (and possibly annealing) underscores the need for a better understanding of the mechanisms that generate damage as well as field measurements that characterize the spatial distribution of damage.

The effects of topographic stress and rock fractures on landscape evolution may extend beyond bedrock erodibility. Spatial trends in fracture abundance and orientation may create characteristic patterns of permeability, and therefore infiltration

and shallow groundwater flow may vary systematically across drainage basins. Reduction of rock strength and enhancement of rock surface area and groundwater flow by fractures should also influence rates of chemical weathering and soil production. As more observations of the subsurface become available, comparisons with modeled stresses will reveal the extent to which topographic stresses shape the deep critical zone.

## Summary and Conclusions

We used a two-dimensional boundary element method to calculate elastic stresses beneath an arbitrary topographic profile due to the combined effects of gravity and tectonics. Calculated stresses and macroscopic fracture patterns for a range of hypothetical profiles across ridges and valleys reveal how the modes and spatial extents of predicted fractures depend on both the ambient tectonic stress and the shape of the topography. In the presence of large regional horizontal compression, the expected fracture mode in the subsurface is typically shear based on a Mohr–Coulomb criterion, with the greatest potential for shear fracture in a shallow zone beneath the valley floor and adjacent slopes. The minimum cohesion needed to prevent shear failure,  $C_{\min}$ , serves as a proxy for the susceptibility of the rock to the formation or reactivation of shear fractures. We used the boundary element method and estimates of regional tectonic stresses to calculate stresses beneath a topographic cross section through the Susquehanna Shale Hills Critical Zone Observatory, an experimental watershed in Pennsylvania, USA. The model predicts a steep decline in  $C_{\min}$  with increasing depth beneath the valley floor, which compares well with a measured decline in the abundance of fractures mapped from optical image logs of four boreholes in the valley. The similarity of these trends is consistent with the hypothesis that topographic stresses influence the formation or reactivation of fractures, and it suggests that feedbacks between topographic stress, rock fracture, and landscape evolution may occur. Future observations of fractures in different topographic settings or in sites with different topographic, lithologic or tectonic characteristics would provide a more complete test of the topographic fracture hypothesis, and could rule out or support alternative explanations for the measured trend in fracture abundance. In sites where topographic stresses influence rock fracture, the model presented here provides a framework for studying the effects of topography on subsurface hydrology and rock weathering, as well as possible feedbacks between rock fracture and landform evolution.

**Acknowledgements**—We thank Carole Johnson for assistance with WellCAD software, Terryl Daniels for field assistance in collecting the OTV logs, Tim White for discussion of the SSHO geology, and Oliver Heidbach for assistance with the sources used to compile the World Stress Map database. We are also grateful to Rick Allmendinger for making his stereonet software freely available. We thank the special issue editors and three anonymous reviewers for their suggestions. This work was supported by the US Army Research Office through award W911NF-14-1-0037 to J.T.P. M.S. was supported by US Department of Energy award DE-FG01-97ER14760 to Brian Evans. Financial Support for the Susquehanna Shale Hills Critical Zone Observatory was provided by National Science Foundation Grants EAR-0725019, EAR-1239285, and EAR-1331726. Research was conducted at the Penn State Stone Valley Forest which is funded by the Penn State College of Agriculture Sciences, Department of Ecosystem Science and Management and managed by the staff of the Forestlands Management Office. Any opinions, findings and conclusions or recommendations expressed in this material are those of the authors and do not necessarily reflect the views of the US Army, the National Science Foundation, or the Department of Energy.



## References

- Anderson SP, von Blanckenburg F, White AF. 2007. Physical and chemical controls on the critical zone. *Elements* **3**(5): 315–319. DOI: 10.2113/gselements.3.5.315
- Augustinus PC. 1995. Glacial valley cross-profile development: the influence of in situ rock stress and rock mass strength, with examples from the Southern Alps, New Zealand. *Geomorphology* **14**(2): 87–97. DOI: 10.1016/0169-555X(95)00050-X
- Berkowitz B. 2002. Characterizing flow and transport in fractured geological media: a review. *Advances in Water Resources* **25**(8): 861–884.
- Borchers JW. 1996. Ground-water resources and water-supply alternatives in the Wawona area of Yosemite National Park, California. United States Geological Survey Water Resource Investigation Report 95–4229.
- Chigara M. 2000. Micro-sheeting of granite and its relationship with landsliding after the heavy rainstorm in June, 1999, Hiroshima Prefecture, Japan. *Engineering Geology* **59**: 219–231.
- Clarke BA, Burbank DW. 2010. Bedrock fracturing, threshold hillslopes, and limits to the magnitude of bedrock landslides. *Earth and Planetary Science Letters* **297**: 577–586.
- Clarke BA, Burbank DW. 2011. Quantifying bedrock-fracture patterns within the shallow subsurface: Implications for rock mass strength, bedrock landslides, and erodibility. *Journal of Geophysical Research* **116**: F04009. DOI: 10.1029/2011JF001987
- Crouch SL, Starfield AM. 1983. *Boundary Element Methods in Solid Mechanics*. Allen and Unwin Ltd: UK.
- Dühnforth M, Anderson RS, Ward D, Stock GM. 2010. Bedrock fracture control of glacial erosion processes and rates. *Geology* **38**: 423–426. DOI: 10.1130/G30576.1
- Gomberg J, Ellis M. 1994. Topography and tectonics of the central New Madrid seismic zone: Results of numerical experiments using a three-dimensional boundary-element program. *Journal of Geophysical Research* **99**: 20299–20310.
- Goodman RE. 1989. *Introduction to Rock Mechanics*, 2nd edn. Wiley: New York. ISBN: 978-0-471-81200-5
- Haimson BC. 1974. A simple method for estimating in situ stresses at great depths. *Field Testing and Instrumentation of Rock*. American Society for Testing Materials: Philadelphia, PA.
- Haimson BC. 1983. A comparative study of deep hydrofracturing and overcoring stress measurements at six locations with particular interest to the Nevada Test Site. In *Hydraulic Fracturing Stress Measurements*. US National Academies Press: Washington, D.C.; 107–118.
- Haimson BC, Doe T. 1983. State of stress, permeability and fractures in the Precambrian granite of northern Illinois. *Journal of Geophysical Research* **88**: 7355–7371.
- Heidbach O, Tingay M, Barth A, Reinecker J, Kurfes D, Müller B. 2008. The World Stress Map database release 2008. DOI: 10.1594/GFZ.WSM.Rel2008
- Holzhausen GR. 1977. Sheet structure in rock and some related problems in rock mechanics. PhD Dissertation. Department of Applied Earth Sciences, Stanford University: Stanford, CA.
- Iverson RM, Reid ME. 1992. Gravity-driven groundwater flow and slope failure potential, 1. Elastic effective-stress model. *Water Resources Research* **28**(3): 925–938.
- Jaeger JC, Cook NGW, Zimmerman RW. 2007. *Fundamentals of Rock Mechanics*, 4th edn. Blackwell Publishing: USA.
- Jin L, Ravella R, Ketchum B, Bierman PR, Heaney P, White T, Brantley SL. 2010. Mineral weathering and elemental transport during hillslope evolution at the Susquehanna/Shale Hills Critical Zone Observatory. *Geochimica et Cosmochimica Acta* **74**: 3669–3691.
- Keller CK, Kamp GVD, Cherry JA. 1986. Fracture permeability and groundwater flow in clayey till near Saskatoon, Saskatchewan. *Canadian Geotechnical Journal* **23**(2): 229–240.
- Kuntz B, Rubin S, Berkowitz B, Singha K. 2011. Quantifying solute transport behavior at the Shale Hills Critical Zone Observatory. *Vadose Zone Journal* **10**: 843–857. DOI: 10.2136/vzj2010.0130
- LeGrand HE. 1949. Sheet structure, a major factor in the occurrence of ground water in the granites of Georgia. *Economic Geology and Bulletin Society of Economic Geologists* **44**: 110–118.
- Leith K, Moore JR, Amann F, Loew S. 2013a. Sub-glacial extensional fracture development and implications for Alpine valley evolution. *Journal of Geophysical Research*. DOI: 10.1002/2012JF002691
- Leith K, Moore JR, Amann F, Loew S. 2013b. *In situ* stress control on micro-crack generation and macroscopic extensional fracture in exhuming bedrock. *Journal of Geophysical Research*. DOI: 10.1002/2012JB009801
- Lo KY. 1981a. Ontario Hydro, Darlington Generating Station A, Rock Stress Measurements and Evaluations: Report 1, Results Of Initial Stress Measurements. Ontario Hydro Report No. 81102, 12.
- Lo KY. 1981b. Ontario Hydro, Darlington Generating Station A, Rock Stress Measurements and Evaluations: Report 3, Evaluation Of Regional Stress Condition. Ontario Hydro Report No. 81282, 12.
- Luthi SM. 2001. *Geological Well Logs: use in Reservoir Modeling*. Springer-Verlag: Berlin.
- Martel SJ. 1999. Analysis of fracture orientation data from boreholes. *Environmental and Engineering Geoscience* **5**: 213–233.
- Martel SJ. 2000. Modeling elastic stresses in long ridges with the displacement discontinuity method. *Pure and Applied Geophysics* **157**: 1039–1057.
- Martel SJ. 2006. Effect of topographic curvature on near-surface stresses and application to sheeting joints. *Geophysical Research Letters* **33**: L01308. DOI: 10.1029/2005GL024710
- Martel SJ. 2011. Mechanics of curved surfaces, with application to surface-parallel cracks. *Geophysical Research Letters* **30**: L20303. DOI: 10.1029/2011GL049354
- Martel SJ, Langley JS. 2006. Propagation of normal faults to the surface in basalt, Koae fault system, Hawaii. *Journal of Structural Geology* **28**: 2123–2143.
- Martel SJ, Muller JR. 2000. A two-dimensional boundary element method for calculating elastic gravitational stresses in slopes. *Pure and Applied Geophysics* **157**: 989–1007.
- McNutt M. 1980. Implications of regional gravity for state stress in the earth's crust and upper mantle. *Journal of Geophysical Research* **85**: B11, 6377–6396.
- McTigue DF, Mei CC. 1981. Gravity-induced stresses near topography of small slope. *Journal of Geophysical Research* **86**(B10): 9268–9278.
- Miller DJ, Dunne T. 1996. Topographic perturbations of regional stresses and consequent bedrock fracturing. *Journal of Geophysical Research* **101**(B11): 25,523–25,536.
- Mitchell KJ. 2010. Factors contributing to the formation of sheeting joints: A study of sheeting joints on a dome in Yosemite National Park. MS Thesis, University of Hawaii at Manoa.
- Molnar P. 2004. Interactions among topographically induced elastic stress, static fatigue, and alley incision. *Journal of Geophysical Research* **109**: F02010. DOI: 10.1029/2003JF000097
- Molnar P, Anderson RS, Anderson SP. 2007. Tectonics, fracturing of rock, and erosion. *Journal of Geophysical Research* **112**: F03014. DOI: 10.1029/2005JF000433
- Moon BP, Selby MJ. 1983. Rock mass strength and scarp forms in southern Africa. *Geography Annals, Series A* **65**(1/2): 135–145. DOI: 10.2307/520727
- Moore JR, Sanders JW, Dietrich WE, Glaser SD. 2009. Influence of rock mass strength on the erosion rate of alpine cliffs. *Earth Surface Processes and Landforms* **34**: 1339–1352. DOI: 10.1002/esp.1821
- Morin RH, Savage WZ. 2002. Topographic stress perturbations in southern Davis Mountains, west Texas, 2, Hydrogeologic implications. *Journal of Geophysical Research* **107**(B12): 2340. DOI: 10.1029/2001JB000488
- Morin RH, Savage WZ, Rivard C. 2006. Hydrologic consequences of gravity-induced stresses along a ridge - example from Annapolis Valley, Nova Scotia: Proceedings, 41st US Symposium on Rock Mechanics, June 17–21. American Rock Mechanics Association, paper no. 1054, Golden, CO.
- Muller JR, Martel SJ. 2000. Numerical models of translational landslide rupture surface growth. *Pure Applied Geophysics* **157**: 1009–1038.
- Muskhelishvili NI. 1953. *Some Basic Problems of the Mathematical Theory of Elasticity*, 4th edn. P. Noordhoff Ltd: The Netherlands.
- Neuman SP. 2005. Trends, prospects and challenges in quantifying flow and transport through fractured rocks. *Hydrogeology Journal* **13**(1): 124–147.
- Overbey WK Jr, Rough RL. 1968. Surface studies orientation of induced formation fractures. *Production Monthly* **32**(8): 16–19.
- Palmer JHL, Lo KY. 1976. *In situ* stress measurements in some near-surface rock formations, Thorold, Ontario. *Canadian Geotechnical Journal* **13**: 1–7.

- Pan E, Amadei B. 1994. Stresses in an anisotropic rock mass with irregular topography. *Journal of Engineering Mechanics* **120**: 97–119.
- Paterson MS, Wong TF. 2005. *Experimental Rock Deformation: The Brittle Field*, 2nd edn. Springer: New York.
- Pollard DD, Fletcher RC. 2005. *Fundamentals of Structural Geology*. Cambridge University Press: Cambridge.
- Portenga EW, Bierman PR. 2011. Understanding Earth's eroding surface with  $^{10}\text{Be}$ . *GSA Today* **21**(8): 4–10.
- Ramsey JM, Chester FM. 2004. Hybrid fracture and the transition from extension fracture to shear fracture. *Nature* **428**: 63–66.
- Savage WZ, Morin RH. 2002. Topographic stress perturbations in southern Davis Mountains, west Texas. 1. Polarity reversal of principal stresses. *Journal of Geophysical Research* **107**(B12): 2339. DOI: 10.1029/2001JB000484
- Savage WZ, Swolfs HS. 1986. Tectonic and gravitational stress in long symmetric ridges and valleys. *Journal of Geophysical Research* **91**: 3677–3685.
- Savage WZ, Swolfs HS, Powers PS. 1985. Gravitational stresses in long symmetric ridges and valleys. *International Journal of Rock Mechanics and Mining Sciences and Geomechanics Abstracts* **22**: 291–302.
- Scheidegger AE. 1963. On the tectonic stresses in the vicinity of a valley and mountain range. *Proceedings of the Royal Society Victoria* **76**: 141–145.
- Serra O. 1989. *Formation MicroScanner Image Interpretation*. Schlumberger Educational Services: Houston, TX.
- Stock GM, Martel SJ, Collins BD, Harp EL. 2012. Progressive failure of sheeted rock slopes: the 2009–2010 Rhombus Wall rock falls in Yosemite Valley, California, USA. *Earth Surface Processes and Landforms* **37**: 546–561. DOI: 10.1029/2011GL049354
- Terzaghi K. 1962. Dam foundation on sheeted granite. *Geotechnique* **12**: 199–208.
- Terzaghi RD. 1965. Sources of error in joint surveys. *Geotechnique* **15**(3): 287–304.
- Thomas AL. 1993. Poly3D: a three-dimensional, polygonal element, displacement discontinuity boundary element computer program with applications to fractures, faults, and cavities in the Earth's crust. MS Thesis, Stanford University.
- Timoshenko SP, Goodier JN. 1970. *Theory of Elasticity*, 3rd edn. McGraw-Hill: New York.
- Trainer FW. 1988. Hydrogeology of the plutonic and metamorphic rocks. In *The Geology of North America*, vol. **O2**, Hydrogeology, Back W *et al.* Geological Society of America: Boulder, CO; 367–380.
- Whipple KX, Hancock GS, Anderson RS. 2000. River incision into bedrock: mechanics and relative efficacy of plucking, abrasion, and cavitation. *Geological Society of America Bulletin* **112**: 490–503. DOI: 10.1130/0016-7606(2000)112<490:RIIBMA>2.0.CO;2
- Wieczorek GF, Snyder JB. 1999. Rock falls from Glacier Point above Camp Curry, Yosemite National Park, California. United States Geological Survey Open File Report 99–385.